

# Magma–Carbonate Interaction Processes and Associated CO<sub>2</sub> Release at Merapi Volcano, Indonesia: Insights from Experimental Petrology

F. M. DEEGAN<sup>1,\*</sup>, V. R. TROLL<sup>1,2</sup>, C. FREDA<sup>2</sup>, V. MISITI<sup>2</sup>,  
J. P. CHADWICK<sup>3</sup>, C. L. McLEOD<sup>4</sup> AND J. P. DAVIDSON<sup>4</sup>

<sup>1</sup>DEPARTMENT OF EARTH SCIENCES, UPPSALA UNIVERSITY, VILLAVÄGEN 16, 75236 UPPSALA, SWEDEN

<sup>2</sup>ISTITUTO NAZIONALE DI GEOFISICA E VULCANOLOGIA, 00143 ROME, ITALY

<sup>3</sup>DEPARTMENT OF PETROLOGY (FALW), VRIJE UNIVERSITEIT, 1081 HV AMSTERDAM, THE NETHERLANDS

<sup>4</sup>DEPARTMENT OF EARTH SCIENCES, THE UNIVERSITY OF DURHAM, DURHAM DH1 3LE, UK

RECEIVED MAY 22, 2009; ACCEPTED FEBRUARY 25, 2010

*There is considerable evidence for continuing, late-stage interaction between the magmatic system at Merapi volcano, Indonesia, and local crustal carbonate (limestone). Calc-silicate xenoliths within Merapi basaltic-andesite eruptive rocks display textures indicative of intense interaction between magma and crustal carbonate, and Merapi feldspar phenocrysts frequently contain crustally contaminated cores and zones. To resolve the interaction processes between magma and limestone in detail we have performed a series of time-variable decarbonation experiments in silicate melt, at magmatic pressure and temperature, using a Merapi basaltic-andesite and local Javanese limestone as starting materials. We have used in situ analytical methods to determine the elemental and strontium isotope composition of the experimental products and to trace the textural, chemical, and isotopic evolution of carbonate assimilation. The major processes of magma–carbonate interaction identified are: (1) rapid decomposition and degassing of carbonate; (2) generation of a Ca-enriched, highly radiogenic strontium contaminant melt, distinct from the starting material composition; (3) intense CO<sub>2</sub> vesiculation, particularly within the contaminated zones; (4) physical mingling between the contaminated and unaffected melt domains; (5) chemical mixing between melts. The experiments reproduce many of the features of magma–carbonate interaction observed in the natural Merapi xenoliths and feldspar phenocrysts. The Ca-rich, high <sup>87</sup>Sr/<sup>86</sup>Sr contaminant melt produced in the experiments is considered as a precursor to the Ca-rich (often*

*‘hyper-calcic’) phases found in the xenoliths and the contaminated zones in Merapi feldspars. The xenoliths also exhibit micro-vesicular textures that can be linked to the CO<sub>2</sub> liberation process seen in the experiments. This study, therefore, provides well-constrained petrological insights into the problem of crustal interaction at Merapi and points toward the substantial impact of such interaction on the volatile budget of the volcano.*

KEY WORDS: carbon dioxide; experimental petrology; magma–carbonate interaction; Merapi; strontium isotopes

## INTRODUCTION

Volcanoes sited above subduction zones are the most dangerous on the planet. Merapi volcano in Central Java, Indonesia, is one such hazardous volcano with both historical and geologically recent explosive eruptions (Voight *et al.* 2000, and references therein; Donoghue *et al.*, 2009). Merapi is one of the most active volcanoes in Java and is located less than 30 km north of Yogyakarta, the largest city in Central Java with a population of *c.* 3.5 million (Fig. 1a and b).

The role of intra-crustal contamination in volcanic arc settings is a source of continuing debate (e.g. Davidson

\*Corresponding author. E-mail: Frances.Deegan@geo.uu.se.

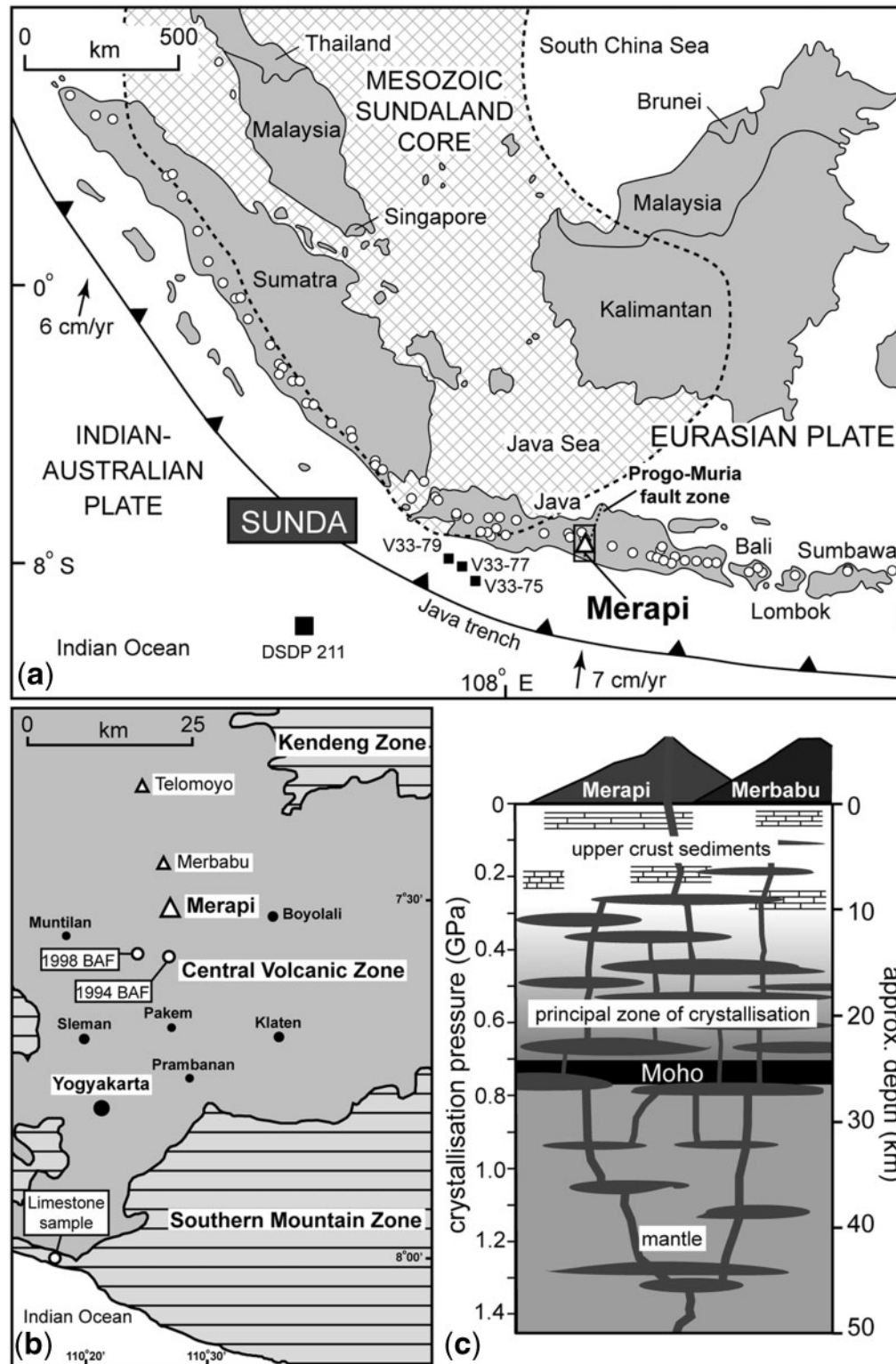


**Fig. 1.** (a) Overview map of the Sunda arc, Indonesia. Open circles represent volcanic centres; Merapi volcano (Central Java) is labelled. Cross-hatched area is Mesozoic continental crust (Sundaland), which probably extends as far as Central Java. Map is modified after Gertisser & Keller (2003) using crustal boundaries from Smyth *et al.* (2007) and references therein. (b) Simplified map of the area surrounding Merapi and Merbabu volcanoes [corresponds to the box in (a)], showing the major geological zones bounding the Central Volcanic Zone (see text for further explanation). Sample locations for this study are indicated (1998 and 1994 xenolith-bearing block and ash flows (BAF) on the south flanks of Merapi and the limestone sample site at Parangtritis beach, south of Merapi). Significant population centres in the vicinity of Merapi are also shown, the largest of which is Yogyakarta *c.* 25–30 km to the south. (c) Schematic section through the crust and mantle beneath Merapi to 50 km depth, showing a hypothetical interconnected network of magma chambers beneath the volcano. Sketch is modified after Chadwick (2008), based on a combination of 3D seismic tomography and pyroxene + amphibole barometry data (see text for details).

*et al.*, 2005). Its occurrence, however, has been well documented at many volcanic centres located in arc settings such as the Lesser Antilles arc (e.g. Smith *et al.*, 1996; Macdonald *et al.*, 2000, and references therein), the Kermadec arc (e.g. Macpherson *et al.*, 1998; Smith *et al.*, 2006), and the Sunda arc in Indonesia (e.g. Gasparon *et al.*, 1994; Gasparon & Varne, 1998).

Merapi is an arc volcano beneath which the upper crust consists of Cretaceous to Tertiary limestone, marl, and volcanoclastic units up to 2 km thick (van Bemmelen, 1949). Sedimentary units in the Central Java area extend to greater depths and the currently active central Javan volcanic arc is partly sited on the Kendang sedimentary basin, in which the sediment thickness ranges from 8 to 11 km (Smyth *et al.*, 2005, and references therein). The upper crustal sediments overlie a basement, of uncertain character, extending to a depth of *c.* 25 km (Curry *et al.*, 1977; Hamilton, 1979). Recent erupted products at Merapi display strong evidence for magma–crust interaction (Chadwick *et al.*, 2007), including the presence of abundant calc-silicate xenoliths, which frequently exhibit well-developed, skarn-type, vesicular reaction rims. Crystal isotope stratigraphy and major element profiling of plagioclase phenocrysts in recent Merapi basaltic-andesites has identified carbonate assimilation and xenolith recycling as a process affecting magma compositions and potentially the volatile budget at Merapi (Chadwick *et al.*, 2007). Merapi feldspars described by Chadwick *et al.* (2007) are variably zoned: (1) plagioclases with albitic cores mantled by anorthitic rims (An<sub>80–90</sub>), with radiogenic <sup>87</sup>Sr/<sup>86</sup>Sr in the rims, which indicate the presence of a Ca-rich, crustally derived melt during their crystallization; (2) plagioclases with anorthitic cores (up to almost An<sub>100</sub>) and crustal <sup>87</sup>Sr/<sup>86</sup>Sr ratios in the cores but less calcic and less radiogenic rim compositions. These latter types are interpreted as inherited, calc-silicate derived crystal cores. It should be noted that magma–carbonate interaction of similar character has also been identified at other volcanic systems emplaced within carbonate-rich crust, such as the Alban Hills, Italy (Freda *et al.*, 1997; Dallai *et al.*, 2004), Vesuvius, Italy (Del Moro *et al.*, 2001; Gilg *et al.*, 2001; Fulignati *et al.*, 2004), and Popocatepetl volcano, Mexico (Goff *et al.*, 2001; Schaaf *et al.*, 2005), all of which, like Merapi, are prone to explosive eruptive behaviour.

Although considerable textural and geochemical ‘end-product’ evidence for interaction between Merapi magmas and crustal carbonates exists, detailed understanding of the mechanisms and rates of magma–carbonate interaction producing such textures and the associated chemical exchanges at the magma–crust interface is very limited. To address this problem, we have designed a time-constrained experimental series to investigate the decarbonation and contamination processes involved in magma–carbonate interaction in a controlled laboratory

environment. Experimental petrology techniques have previously been used to examine processes of assimilation and contamination in magmatic systems (e.g. Watson, 1982; Watson & Jurewicz, 1984; Johnston & Wyllie, 1988; Beard *et al.*, 1993; Sachs & Strange, 1993; McLeod & Sparks, 1998; Knesel & Davidson, 2002; García-Moreno *et al.*, 2006); however, our experimental design differs significantly from previous works in two key aspects. First, we focus on assimilation of crustal carbonate by magma, which is less frequently addressed in the literature than fusion and assimilation of silicic crustal components. Some experimental studies of limestone assimilation by magma have been carried out previously, but in contrast to the present study they have largely focused on the phase assemblages resulting from carbonate digestion, rather than on the initial processes and progression of carbonate assimilation (see Freda *et al.*, 2008a; Iacono Marziano *et al.*, 2008; Mollo *et al.*, 2010). Second, we have carried out experiments using very short and progressively increasing dwell times (0–300s), much shorter than those of any other experimental study of xenolith assimilation in the literature, in which experiments typically run for hours to days. These design considerations allow for preservation of transient textures in the experimental products and for examination of some features of mass transport and intra-melt homogenization at the contaminated melt front as carbonate assimilation proceeds. We have carried out piston-cylinder experiments at  $T=1200^{\circ}\text{C}$  and  $P=0.5\text{ GPa}$ , which corresponds to a relatively deep-seated system (15–20 km) compared with the setting where carbonate assimilation is largely expected to occur (in the upper 10 km of the crustal section beneath Merapi, Fig. 1c). We applied a pressure of 0.5 GPa as this is the lowest pressure that the piston-cylinder apparatus is calibrated for. Our system hence closely simulates the deepest conditions under which carbonate assimilation might initiate and our results can, in turn, be sensibly extrapolated to a shallower system. With respect to the rate of decarbonation, this will proceed considerably faster under lower pressures. This means that the timescales of carbonate assimilation estimated from our experiments represent a maximum of what we can expect in nature under similar conditions to our experimental system.

In our experiments the limestone contaminant is heated concurrently with the starting powdered glass (M-94-a-107), which may initially appear to represent a thermal limitation to this approach. Considering some aspects of the magmatic system at Merapi, however, such as its long-lived nature (the onset of volcanism is estimated at 40 ka BP; Camus *et al.*, 2000) and its high heat flux (Koulakov *et al.*, 2007; Wagner *et al.*, 2007; Chadwick, 2008), the crust underlying Merapi must be already heated to several hundred degrees Celsius. We argue that simultaneous heating of the starting materials in our

experiments therefore best simulates a long-lived system, such as Merapi (Annen & Sparks, 2002).

By considering the experimental data in combination with the natural products of magma–carbonate interaction (xenoliths and feldspars), we can improve our understanding of both deep and shallow crustal contamination processes. The experiments provide insights into the late-stage, short-timescale decarbonation processes that can seriously affect the eruptive behaviour of volcanoes located on carbonate crust with potentially very little forewarning.

## GEOLOGICAL BACKGROUND

Merapi volcano is located within the active Sunda arc, in Central Java, Indonesia (Fig. 1a). Northward subduction of the Indian Ocean plate beneath the Eurasian plate has been occurring along the Java trench since the middle Eocene (Hamilton, 1979; Hall, 2002). This has resulted in an ancient Eocene to Miocene volcanic zone in the southern part of Java known as the Southern Mountain Zone, and the present-day volcanic arc that is distributed along the entire length of the central part of the island, known as the Central Volcanic Zone (Smyth *et al.*, 2007). Van Bemmelen (1949) described several stratigraphic–tectonic zones within Java, of which the major zones, from south to north, are: the Southern Mountain Zone, the Central Volcanic Zone, the Kendeng Zone and the Rembang Zone. The currently active Central Volcanic Zone is partly sited on the Kendeng Zone, which is the main Eocene–Miocene sedimentary basin in East Java, comprising 8–11 km thick successions of volcanoclastic and marine sediments, including abundant limestone units up to 2 km thick (van Bemmelen, 1949; de Genevraye & Samuel, 1972; Untung & Sato, 1978; Smyth *et al.*, 2005). Merapi is the youngest of a cross-arc NNW–SSE-trending chain of volcanoes, including Telemoyo, Merbabu, and Merapi, which are bound by the Southern Mountain and Kendeng Zones (Fig. 1b). The nature of the basement beneath Merapi is intermediate between oceanic and continental crust (Curry *et al.*, 1977), with Merapi sited close to a structural lineation referred to as the Progo–Muria fault, thought to delimit the extent of Cretaceous continental basement beneath Java (Smyth *et al.*, 2005; Fig. 1a). Geobarometric and tomographic methods applied to Merapi volcano and its basement by Chadwick (2008) indicate that an interconnected network of melt bodies is likely to exist beneath the edifice in a diffuse zone from a depth of *c.* 3 km to *c.* 31 km beneath the summit (summit elevation is *c.* 3000 m) (Fig. 1c). Such a magmatic plumbing system beneath the volcano provides ample opportunity for interaction between magma and upper- to mid-crustal lithologies, including abundant carbonate rocks in the top 10 km.

Of the 89 Indonesian volcanoes with historical eruptions (van Bemmelen, 1949), Merapi is one of the most active

and destructive. Recent volcanism at Merapi is characterized by the growth of viscous lava domes followed by collapse of the dome complex and resultant pyroclastic block and ash flows (BAFs or *nuées ardentes*; e.g. Abdurachman *et al.*, 2000; Schwarzkopf *et al.*, 2001, 2005; Charbonnier & Gertisser, 2008; Donoghue *et al.*, 2009). The volcanic products are basaltic-andesite in composition and contain abundant xenolithic inclusions, among which thermally metamorphosed calc-silicate types are common (e.g. Clochiatti *et al.*, 1982; Camus *et al.*, 2000, and references therein). The various types of inclusion hosted within the Merapi lavas have been described by Troll *et al.* (2003) and a detailed petrographic and geochemical description of a selection of typical Merapi calc-silicate xenoliths, including those presented here, has been given by Chadwick *et al.* (2007). Hand-specimen examples of the xenoliths described in this study, with distinctive macroscopic features such as vesicular textures and neo-mineralized skarn contact zones between magma and xenolith, are shown in Fig. 2. The presence of such metamorphosed limestone xenoliths was the primary motivation for our experimental study, as they indicate continuing, albeit poorly constrained, magma–carbonate interaction beneath Merapi, which we hypothesize has significant repercussions for the volcano's short-term volatile budget and consequent eruptive behaviour.

## EXPERIMENTAL METHODS

All of the experiments in this study were carried out using the piston-cylinder apparatus at the HP–HT Laboratory of Experimental Volcanology and Geophysics at the Istituto Nazionale di Geofisica e Vulcanologia (INGV) Rome. The piston-cylinder is calibrated to perform experiments in the pressure range 0.5–2 GPa. All experiments reported here were carried out at the lowest end of this range, at 0.5 GPa, which corresponds to a mid-crustal depth of *c.* 15 km (note that the total crustal thickness in Java is *c.* 25 km) (Curry *et al.*, 1977; Hamilton, 1979). Pressures equivalent to shallower crustal depths cannot be simulated using the piston-cylinder apparatus. However, the piston-cylinder has a major advantage over low-pressure experimental devices, which is its rapid heating and quench rate. The piston-cylinder apparatus reaches 1200°C after only 6 min, which is sufficiently fast to allow preservation of the carbonate phase in the shortest duration experiments and subsequent inspection of the interaction between carbonate and melt over a timescale of minutes after the experimental temperature is reached. It is for this reason that the piston-cylinder was selected as the most appropriate instrument for this study. Given that the magmatic system beneath Merapi extends from *c.* 3 km to 31 km depth (Chadwick, 2008), the middle to upper parts of the system must be emplaced into sedimentary sequences that attain thicknesses of up to 11 km

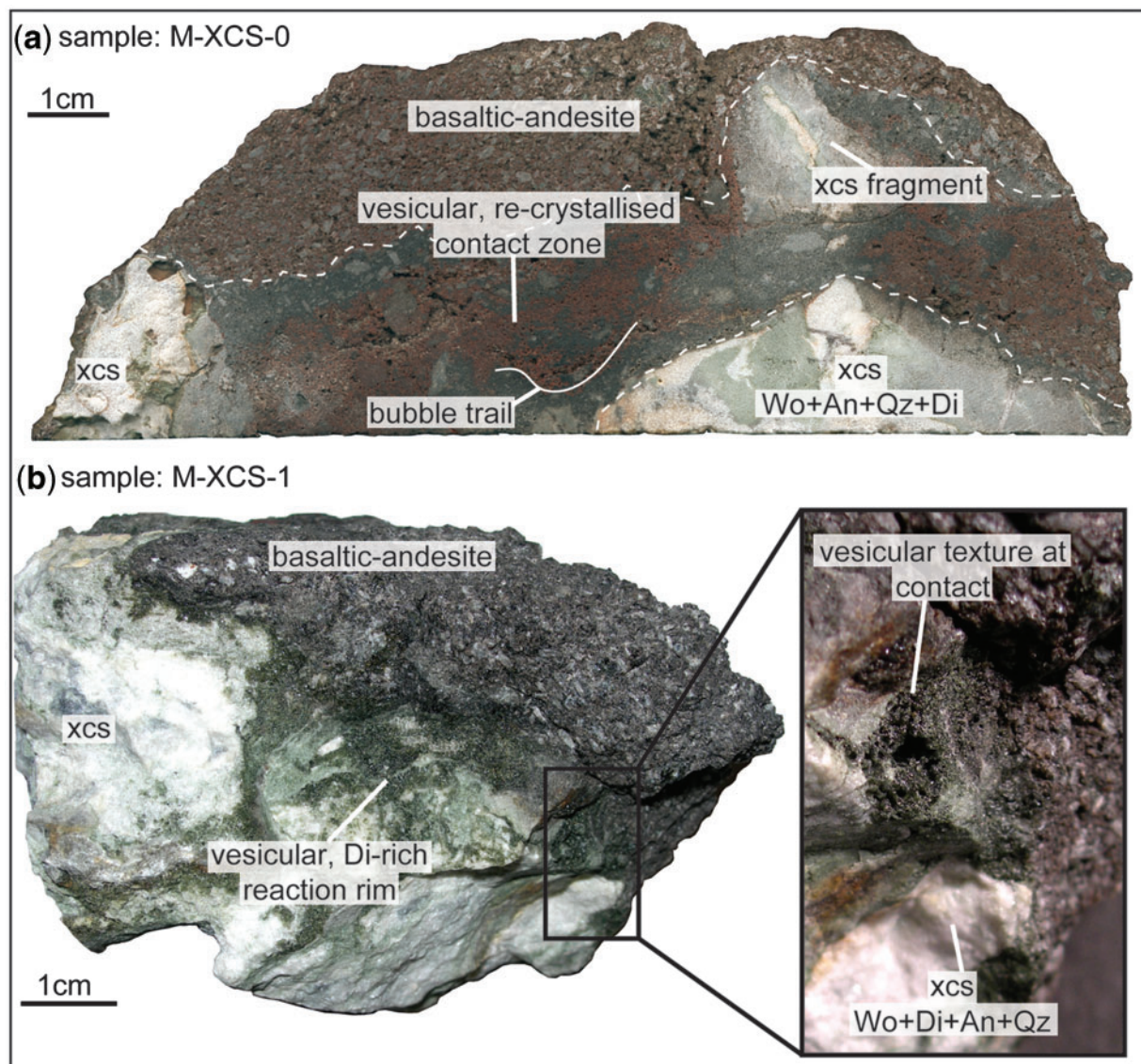


**Fig. 2.** Representative examples of Merapi calc-silicate xenoliths (xcs) from a 1998 block and ash flow (for map location see Fig. 1b) at a hand-specimen scale. Samples display intensely developed xenolith–magma contact zones with vesicular textures and skarn-type mineral assemblages. Wo, wollastonite; Di, diopside; An, anorthite; Qz, quartz. Mineral assemblages listed in figure are in order of decreasing abundance.

(Smyth *et al.*, 2005, and references therein). Our experimental approach, therefore, is a close replication of the physical conditions at which initial magma–carbonate interaction is likely to occur; that is, the deep to mid-level parts of the magma system at Merapi.

### Starting materials

The experimental series was divided into two sub-series that were run in tandem: experiments using a nominally anhydrous starting material and experiments using a hydrated starting material. Each experimental run contained one anhydrous and one hydrated experiment to

allow a direct comparison at each given set of parameters. The starting material for all experiments was a sample of Merapi basaltic-andesite (sample M-94-a-107, courtesy of L. M. Schwarzkopf) from the 1994 block and ash flow deposits. This sample was chosen for use in the experiments as it is representative of the most recent volcanic material produced at Merapi, which is host to many calc-silicate xenoliths. M-94-a-107 is a grey finely crystalline rock with up to 45% phenocrysts by volume, predominantly of plagioclase, with some clinopyroxene and minor amounts of amphibole. The sample was crushed into 1–2 mm sized chips, hand-picked for pristine appearance, and then

Table 1: Composition of starting materials used in the experiments

	Average composition (EMP) of anhydrous M-94-a-107 glass*	1 $\sigma$ (10) <sup>‡</sup>	Average composition (EMP) of hydrous M-94-a-107 glass <sup>†</sup>	1 $\sigma$ (9) <sup>‡</sup>	Whole-rock analysis (XRF) of limestone added <sup>§</sup>
wt %					
SiO <sub>2</sub>	54.11	0.60	51.83	0.43	0.28
TiO <sub>2</sub>	0.85	0.09	0.89	0.05	0.01
Al <sub>2</sub> O <sub>3</sub>	18.98	0.17	18.08	0.24	0.13
FeO	7.89	0.56	8.17	0.16	0.01
MnO	0.24	0.03	0.20	0.03	0.00
MgO	2.98	0.13	2.97	0.08	0.40
CaO	8.89	0.17	9.19	0.16	56.72
Na <sub>2</sub> O	3.56	0.13	3.48	0.09	0.12
K <sub>2</sub> O	2.05	0.10	2.05	0.03	0.00
P <sub>2</sub> O <sub>5</sub>	0.29	0.04	0.34	0.04	0.03
Total	99.85		97.20		57.70
H <sub>2</sub> O	—		2.23		0.15
CO <sub>2</sub>	—		—		44.93

\*Glass synthesized using M-94-a-107 whole-rock powder in a Pt capsule at 1300°C, 1 atm in air.

<sup>†</sup>M-94-a-107 glass uniformly hydrated at Universität Hannover (Germany) and measured for water content by Karl Fischer Titration (KFT).

<sup>‡</sup>1 $\sigma$  standard deviation; the number in parentheses represents the number of analyses for each sample.

<sup>§</sup>XRF analysis carried out at IFM-GEOMAR (Kiel, Germany).

ground to a powder in a WC Tema mill. The powdered sample was subsequently fused, to produce a homogeneous glass of basaltic-andesite composition. The nominally anhydrous glass was produced at the Università degli Studi Roma Tre, Italy by melting an aliquot of the M-94-a-107 powder at 1300°C and 1 atm in a rapid-quench furnace. The hydrous glass, in turn, was produced at the Universität Hannover, Germany by doping the M-94-a-107 powder with *c.* 2 wt % H<sub>2</sub>O and melting in an internally heated pressure vessel at 1200°C at 0.2 GPa. The hydrated glass was analysed for its water content by Karl Fischer Titration (KFT) at Hannover, Germany (for details of the KFT method see Behrens, 1995). Both sets of glass (anhydrous and hydrous) were analysed for their composition (Table 1) and verified to be free of crystals and crystallites by back-scattered electron (BSE) imaging using the electron microprobe at INGV Rome. The glasses were then hand-ground to a powder using an agate mortar and pestle before insertion into the experiment capsules.

The calcium carbonate added to the experimental charges was from a sample of local crust sourced from a carbonate platform south of Merapi, at the town of Parangtritis (see Fig. 1b and Chadwick *et al.*, 2007, for sample location). The limestone sample was cut into cubes of *c.* 3 mm side length (*c.* 9–10 mg) for use in the

experiments. The composition of the carbonate starting material (Table 1) was determined by X-ray fluorescence (XRF) (for major elements) and IR photometry (for CO<sub>2</sub> content) at IFM-GEOMAR, Kiel, Germany following the method given by Abratis *et al.* (2002).

### Experimental conditions and procedure

All of the experiments were carried out at 1200°C and 0.5 GPa (Table 2), except for one experiment run at 1 GPa to test for any additional pressure effects. The dwell time ( $t_d$ ) is the length of time that the experiment was held at the experimental temperature. This parameter was varied from  $t_d = 0$ s (i.e. immediate quenching upon reaching 1200°C) to  $t_d = 300$ s. Experiments were carried out at super-liquidus temperature for the hydrated Merapi basaltic-andesite. This temperature has been used in Merapi assimilation and fractional crystallization models (AFC) by Chadwick *et al.* (2007) and was verified as a super-liquidus temperature here for the hydrated starting composition by running melting experiments, without carbonate, at 1200°C with  $P = 0.5$  GPa and  $t_d = 300$ s. These experiments yielded crystal-free products and are consistent with two-pyroxene thermometry of 1994 Merapi BAF samples presented by Gertisser (2001), which yielded a pyroxene crystallization temperature (sub-liquidus) of  $1007 \pm 12$ °C.

Table 2: *Experimental conditions and phases present in the experiments*

Run-sample	<i>P</i> (GPa)	<i>T</i> (°C)	<i>t</i> <sub>d</sub> * (s)	M-94-a-107 (mg)	CaCO <sub>3</sub> added (mg)	Phases present
379-16	0.5	1200	0	40.5	9.9	S (cc + x), M, V
379-17†	0.5	1200	0	40.4	9.9	S (cc + crys), M, V
387-20	0.5	1200	60	38.3	9.6	S (cc + x), M, V
387-21†	0.5	1200	60	41.7	10.0	S (cc + crys), M, V
376-10	0.5	1200	90	40.9	9.6	S (cc + x), M, V
376-11†	0.5	1200	90	42.9	9.1	M, V
375-6	0.5	1200	150	42.5	10.1	S (cc + x), M, V
375-7†	0.5	1200	150	42.7	10.3	M, V
374-4	0.5	1200	300	40.5	8.5	S (x), M, V
374-5‡	0.5	1200	300	42.6	9.3	M, V
386-18	0.5	1200	300	41.2	9.9	S (x), M, V
386-19†	0.5	1200	300	41.3	9.9	M, V
374-8‡	0.5	1200	300	40.8	0.0	S (x), M, V (μ)
378-15†‡	0.5	1200	300	30.0	0.0	M, V (μ)

\**t*<sub>d</sub> is an abbreviation for the dwell time of an experiment (i.e. the length of time that the experiment is held at 1200°C).

†Experiments carried out using the hydrated M-94-a-107 glass.

‡Control experiments carried out with no added limestone.

S, solid; cc, calcium carbonate; x, plagioclase crystals; crys, calcite crystallites; M, melt; V, volatiles, CO<sub>2</sub> and/or H<sub>2</sub>O; μ, micro-bubbles only.

Platinum capsules with 3.0 mm outer diameter were used for all experiments. The capsules were welded at one end using an arc welder and loaded with the powdered M-94-a-107 glass to fill about one-fifth of the capsule volume. This was followed by insertion of a cube of limestone (8.5–10.3 mg), after which the capsule was loaded with more powdered M-94-a-107 glass (38–42 mg) (see Table 2). The ratio of powder inserted before the carbonate to that inserted after was kept similar for all runs. The capsules were then welded shut and positioned into a 19.1 mm NaCl–crushable alumina–Pyrex assembly, with the capsules containing the hydrated starting material additionally encased in pyrophyllite powder to prevent water loss (see Freda *et al.*, 2001).

Experiments were pressurized at room temperature to 0.5 GPa and then heated in two stages, from ambient temperature to 1180°C at a rate of 200°C/min, followed by gradual heating at 20°C/min until the experimental temperature was reached. Temperature was controlled by a factory calibrated W<sub>95</sub>Re<sub>5</sub>–W<sub>74</sub>Re<sub>26</sub> (type C) thermocouple and held within ±3°C of the experimental temperature. For this type of assembly, the temperature gradient along the capsules is around 10°C (Hudon *et al.*, 1994; Médard *et al.*, 2008). An oxygen fugacity of about NNO + 2 (where NNO is the nickel–nickel oxide buffer) was attained in the experiments, as a result of the type of assembly used to encase the charges (Freda *et al.*, 2008a, and references therein).

Generally, two capsules were inserted into the experiment assembly (one hydrous and one anhydrous); however, for some runs the assembly was constructed to hold three capsules equidistant from the thermocouple ‘hotspot’. This configuration was used to allow, for example, a carbonate-free control experiment to be run under the same conditions as the hydrous and anhydrous decarbonation experiments. Selected runs were repeated to verify the reproducibility of the results.

Experiments were terminated by shutting down the power source. In this way the experimental charges were quenched at a rate of *c.* 2000°C/min (to the glass transition) and the textural interplay between limestone and the melt was preserved. The experimental capsules were then retrieved, mounted in epoxy resin, opened on one side parallel to their long axes, and polished for micro-analytical analysis.

## ANALYTICAL METHODS

### Electron microprobe analysis (EMPA)

Microprobe analyses and BSE images of the experimental products were obtained at INGV Rome, Italy, using a JEOL-JXA8200 energy-dispersive–wavelength-dispersive (EDS-WDS) combined instrument, equipped with five WDS spectrometers and 12 crystals. Microprobe WDS analyses were performed using an accelerating voltage of 15 kV, a beam current of 5 nA, and a beam diameter of

5  $\mu\text{m}$  for glass and 1  $\mu\text{m}$  for mineral analyses (see, e.g. Iezzi *et al.*, 2008, for analytical details). Sodium and potassium were analysed first to reduce loss on volatilization. Analyses and imaging were carried out over several analytical sessions, with standards optimized for each session. Microprobe analyses and BSE images of a representative selection of natural Merapi calc-silicate xenoliths were also obtained at INGV Rome using the same analytical conditions as for the experimental products. The average standard deviation ( $1\sigma$ ) of each element in the analysed standards over five analytical sessions (including both experiment and xenolith analyses) is as follows: 0.28 for  $\text{SiO}_2$ , 1.86 for  $\text{TiO}_2$ , 0.27 for  $\text{Al}_2\text{O}_3$ , 0.47 for  $\text{FeO}$ , 0.33 for  $\text{MnO}$ , 0.44 for  $\text{MgO}$ , 0.33 for  $\text{CaO}$ , 0.41 for  $\text{Na}_2\text{O}$ , 0.26 for  $\text{K}_2\text{O}$ , 0.35 for  $\text{P}_2\text{O}_5$ .

### Micro-sampling and analysis of $^{87}\text{Sr}/^{86}\text{Sr}$ and trace elements

Micro-sampling of the experimental products was carried out in the Arthur Holmes Isotope Geology Laboratory at Durham University, UK, using a New Wave Micromill following the techniques given by Charlier *et al.* (2006) and references therein. The micro-mill apparatus consists of a drill and stage, a binocular microscope, and a computer workstation that integrates all components, allowing for precise control to *c.* 1  $\mu\text{m}$  of the location of the drill points, the movement of the drill, and the depth of drilling. Suitable sampling areas were selected using BSE images of the experimental charges, taking care to avoid fractures and bubbles. Samples were then mounted as thick sections (up to 500  $\mu\text{m}$  thick) prior to micro-milling. The BSE images were used in conjunction with the binocular microscope optics at the drill workstation to locate the optimal sampling areas. Samples were milled in discrete arrays of points to a depth of *c.* 90  $\mu\text{m}$  per sample by performing two passes of 45  $\mu\text{m}$  depth per sample. The size of each sample array varied as a result of nearby bubbles and fractures, which limited the area that could be drilled. Milling was carried out under a drop of ultra-pure Milli-Q water to collect the drilled sample powder. The water and sample powder mixture was then pipetted onto a gold boat and placed in an ultra-clean fume hood to evaporate the water. The sample powder was then dissolved in ultra-pure, distilled acids and the Sr fraction subsequently separated using micro-Sr column chemistry as described by Charlier *et al.* (2006) in preparation for thermal ionization mass spectrometry (TIMS). Procedural blanks were obtained by milling within the water drop, but without touching the sample. The blank was thereafter treated identically to the samples. Samples were analysed at the University of Durham using a Thermo-Finnigan Triton TIMS system operating in static mode. Details of the procedure used to load small Sr samples, TIMS system running conditions, and data correction have been given by Font *et al.* (2008). The Triton was in positive mode

from January to March 2009, during which 78 analyses of the international Sr standard NBS 987 were carried out on loads ranging from 3 to 600 ng. The overall average NBS 987  $^{87}\text{Sr}/^{86}\text{Sr}$  value is  $0.710246 \pm 0.000016$  ( $2\sigma$ ) ( $n = 78$ ), which agrees extremely well with the accepted NBS 987  $^{87}\text{Sr}/^{86}\text{Sr}$  value reported by Thirlwall *et al.* (1991) of  $0.710248 \pm 0.000023$  ( $2\sigma$ ) ( $n = 427$ ). Aliquots of the dissolved samples were also analysed for their trace element concentrations by inductively coupled plasma mass spectrometry (ICP-MS) using a Thermo Electron Element II system at Durham University. Procedural details have been given by Font *et al.* (2008). Total procedural blanks ( $n = 3$ ) were less than 19 pg for all elements analysed; Sr blanks averaged  $0 \pm 1$  pg ( $2\sigma$ ) ( $n = 3$ ). In total, nine glass samples were micro-milled and analysed from two experiments: 379-17 ( $t_d = 0\text{s}$ ;  $n = 4$ ) and 386-19 ( $t_d = 300\text{s}$ ;  $n = 5$ ).

## EXPERIMENTAL RESULTS

The textural progression of magma–carbonate interaction, in both anhydrous and hydrous experiments, is shown in the BSE images in Fig. 3, and a summary of the phases detected in each experiment is given in Table 2. Figure 3a–e shows the major features of magma–carbonate interaction from  $t_d = 0\text{s}$  (immediate quenching at 1200°C) to  $t_d = 300\text{s}$  for experiments carried out using the nominally anhydrous M-94-a-107 starting glass. Figure 3f–j shows the same sequence for experiments carried out using the hydrated ( $\text{H}_2\text{O} = 2.23$  wt %) M-94-a-107 starting glass. The major textural features of carbonate assimilation include the development of copious amounts of gas bubbles and the generation of two compositionally distinct domains of glass, which can be identified on the BSE images by their contrasting brightness. The faster rate of carbonate assimilation in the hydrated series should be noted.

Major element profiles (EMPA) were obtained through the carbonate–glass and the intra-glass interfaces in all experiments, where applicable. Representative element variation profiles are shown in Fig. 4 for hydrous experiments only, because the glass in the hydrous experiments is generally crystal free (only the shorter runs contain calcite crystallites within the Ca-contaminated regions). This allows for examination of the intra-melt transitions, excluding complications caused by crystallization at the interfaces. Furthermore, the hydrous series of experiments more closely represents the natural, ‘wet’ arc-magma system. It is noteworthy, however, that both the anhydrous and the hydrous experiments display similar features in terms of textures, major element composition, and the shapes of the chemical profiles that traverse the glass interfaces. Representative major element analyses of the experimental glasses are given in Table 3. The Sr isotope profiles of two hydrous experiments are shown in Fig. 5 and the data reported in Table 4.

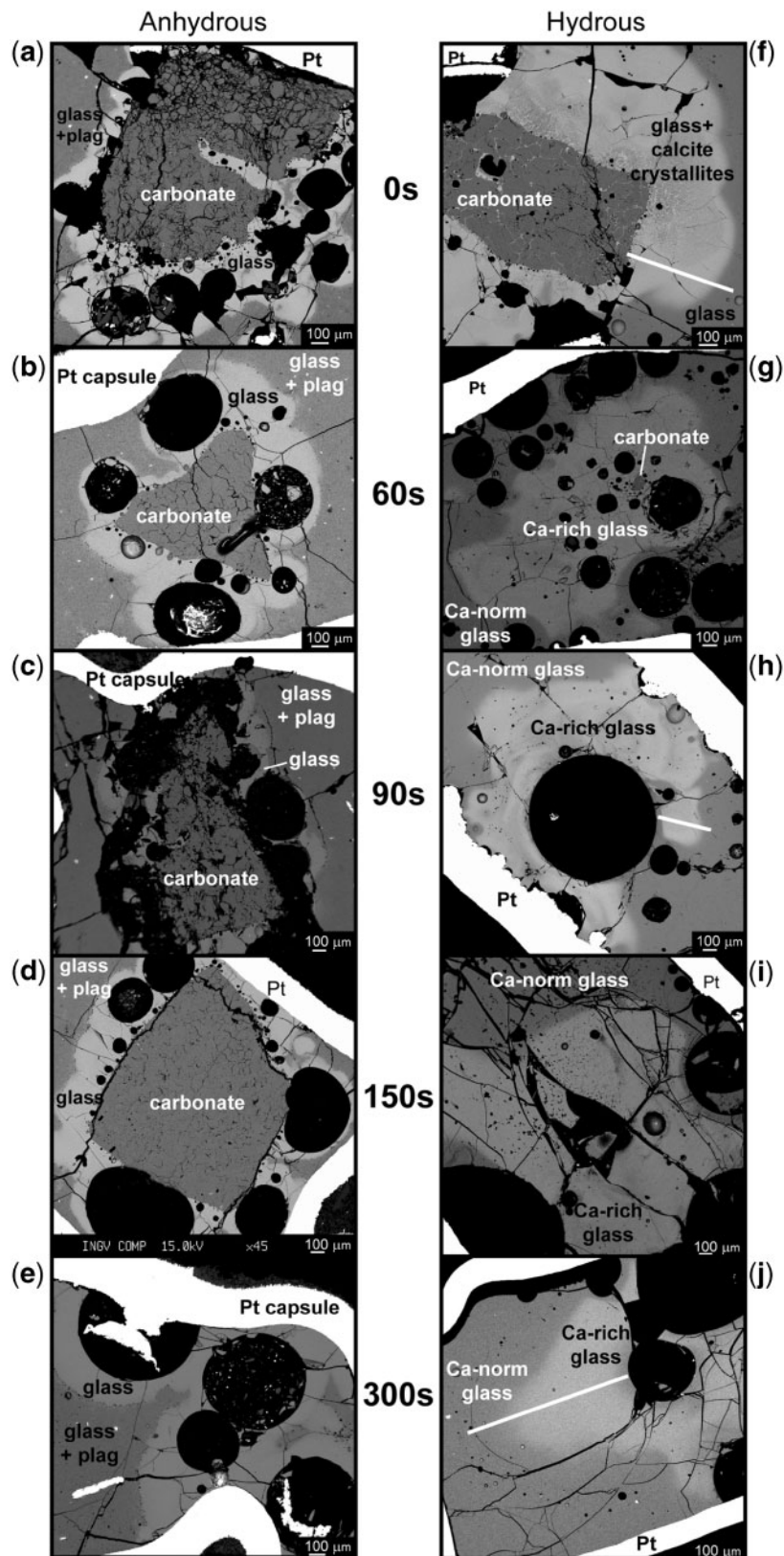


**Fig. 3.** BSE images of the experimental products arranged to show the temporal sequence and major textural features of magma–carbonate interaction in the experiments. The anhydrous (a–e) and hydrous (f–j) experimental series are shown in the left and right columns, respectively. All experiments were carried out at  $T=1200^{\circ}\text{C}$  and  $P=0.5\text{ GPa}$ . The Ca-rich and Ca-normal glass domains can be distinguished by their contrasting brightness in the images, where the bright glass is Ca-rich and the dark grey glass is Ca-normal. Thick white lines in (f), (h) and (j) are EMPA traverses, corresponding to the graphs in Fig. 4.

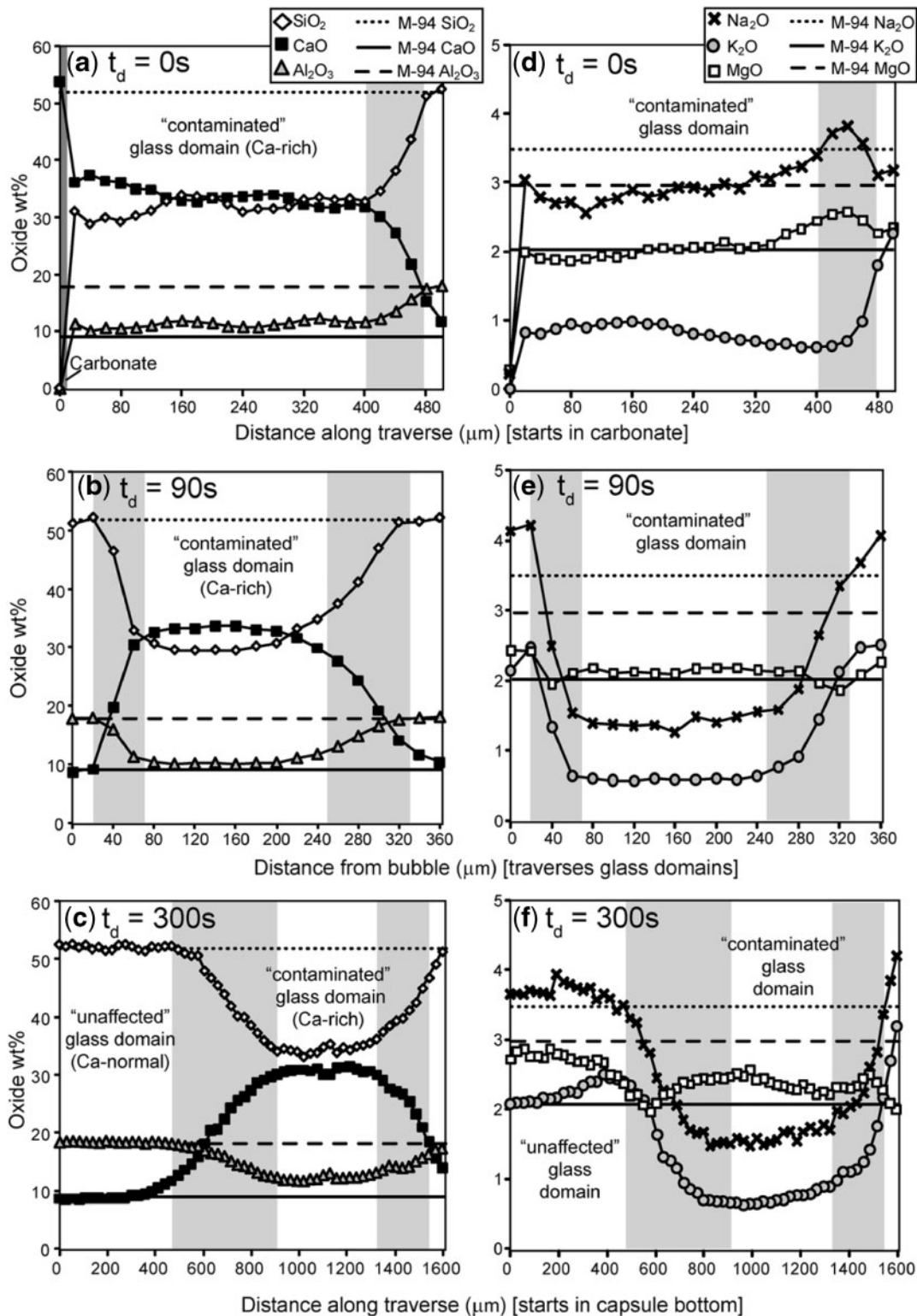


**Fig. 4.** Representative major and minor element chemical profiles in hydrated runs at 0s (a, d), 90s (b, e), and 300s (c, f), respectively. Profiles correspond to the traverses indicated in Fig. 3f, h and j. The glass interfacial region is highlighted with grey shading on the plots. This is the region spanning the Ca-enriched melt–Ca-normal melt contact over which a steady interchange between CaO and  $\text{SiO}_2$  is observed. It should be noted that the glass interfacial region is considerably wider at 300s (c. 450  $\mu\text{m}$  maximum) than at 0s and 90s (c. 80  $\mu\text{m}$  maximum for both).

Table 3: Representative EMP analyses of experimentally derived glasses

Run-sample:	Ca-normal glass				Ca-rich glass			
	379-17	376-11	386-19	374-5	379-17	376-11	386-19	374-5
<i>wt %</i>								
SiO <sub>2</sub>	51.97	51.62	52.28	50.83	34.11	27.72	34.90	38.08
TiO <sub>2</sub>	0.74	0.81	0.77	0.89	0.45	0.49	0.56	0.58
Al <sub>2</sub> O <sub>3</sub>	17.94	18.21	18.50	18.70	12.27	10.32	12.23	13.93
FeO	6.89	6.42	6.30	6.23	5.35	4.85	5.38	5.48
MnO	0.17	0.10	0.10	0.20	0.11	0.18	0.13	0.14
MgO	2.89	2.82	2.66	2.73	2.41	2.18	2.30	2.26
CaO	9.13	8.88	9.75	8.83	31.16	34.34	31.08	27.39
SrO	0.09	0.10	0.08	0.10	0.03	0.08	0.08	0.07
Na <sub>2</sub> O	3.94	4.54	3.66	4.48	1.35	1.33	1.75	2.22
K <sub>2</sub> O	2.40	2.48	2.50	2.26	0.73	0.65	0.79	1.21
P <sub>2</sub> O <sub>5</sub>	0.32	0.28	0.30	0.27	0.22	0.16	0.24	0.22
Total*	96.48	96.26	96.90	95.52	88.19	82.30	89.44	91.56

Run-sample:	Hybrid glass <sup>†</sup>				Inter-carbonate glass			
	379-17	376-11	386-19	375-5	379-17	379-17	379-16	387-21
<i>wt %</i>								
SiO <sub>2</sub>	46.25	41.15	50.72	49.18	31.19	30.23	36.45	34.68
TiO <sub>2</sub>	0.62	0.66	0.64	0.67	0.52	0.44	0.53	0.47
Al <sub>2</sub> O <sub>3</sub>	16.07	14.93	17.73	17.49	10.19	10.40	13.22	13.22
FeO	6.23	5.28	5.05	4.98	4.07	3.81	5.60	4.91
MnO	0.13	0.07	0.13	0.16	0.12	0.07	0.16	0.18
MgO	2.46	2.27	1.96	2.05	2.10	2.15	2.33	2.02
CaO	19.42	24.00	15.64	15.60	35.41	36.52	32.13	32.41
SrO	0.05	0.07	0.04	0.11	0.09	0.01	0.08	0.03
Na <sub>2</sub> O	2.35	2.07	2.81	3.54	2.46	2.60	1.73	1.74
K <sub>2</sub> O	1.33	1.01	2.01	2.18	1.45	1.44	0.89	0.86
P <sub>2</sub> O <sub>5</sub>	0.26	0.20	0.32	0.24	0.25	0.22	0.22	0.21
Total*	95.17	91.71	97.05	96.20	87.85	87.89	93.33	90.70

\*Analysis totals are low (sometimes <90 wt %) as a result of a combination of dissolved volatiles (mainly CO<sub>2</sub>) and unavoidable micro-bubbles.

<sup>†</sup>Glass with composition intermediate between the Ca-normal and Ca-rich end-members. Analyses shown are from the glass interfacial regions.

Trace element concentrations in the drilled samples can be found in the Electronic Appendix (available for downloading at <http://petrology.oxfordjournals.org/>).

### Overview of the experimental products

In the anhydrous series, carbonate is preserved in experiments for  $t_d$  up to 150s (Fig. 3a–d), but appears to be largely consumed at  $t_d > 150$ s (Fig. 3e). Experiments consist of three phases: solid (crystals with or without carbonate), melt (preserved as glass), and an exsolved volatile phase

(CO<sub>2</sub> preserved as vesicles). Crystals of plagioclase (and minor amounts of spinel) always occupy some of the solid phase in the anhydrous experiments, but not in the hydrous ones.

In the hydrous series the rate of carbonate consumption is higher than in the anhydrous experiments, as evidenced by the comparatively smaller amount of carbonate surviving with increasing dwell times. Hydrous experiments for  $t_d \leq 60$ s are similar to their anhydrous counterparts, with three phases detected: solid (carbonate + dendritic calcite

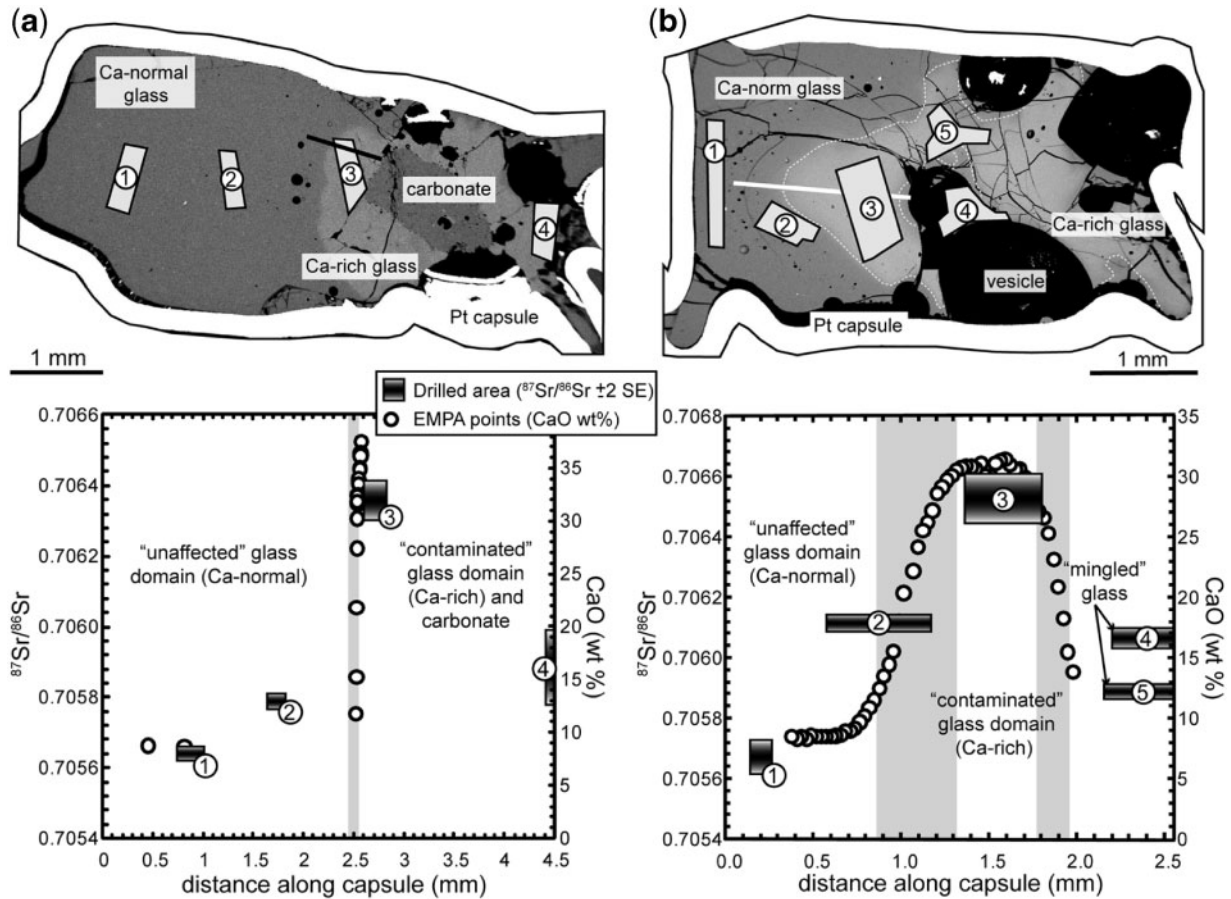


**Fig. 5.**  $^{87}\text{Sr}/^{86}\text{Sr}$  and CaO wt % profiles in (a) a 0s experiment (379-17) and (b) a 300s experiment (386-19). Drilled areas are highlighted in grey on the BSE images (taken prior to drilling), and correspond to the numbered rectangles on the plot. The length of the rectangles corresponds to the area drilled and their height includes  $\pm 2$  SE. Grey shaded vertical bars represent the glass interfacial regions.

**Table 4:** Strontium concentrations and isotope ratios in micro-milled experimental glass

Experiment, location	Sr (ppm)	$^{87}\text{Sr}/^{86}\text{Sr}$	2 SE
<i>379-17 (0s)</i>			
1 (M73-3)	494	0.705641	0.000020
2 (M73-2)	472	0.705788	0.000008
3 (M73-4)	466	0.706361	0.000056
4 (M73-5)	500	0.705886	0.000106
<i>386-19 (300s)</i>			
1 (M73-7)	509	0.705675	0.000056
2 (M73-8)	370	0.706117	0.000020
3 (M73-9)	390	0.706532	0.000082
4 (M73-10)	420	0.706068	0.000030
5 (M73-11)	375	0.705893	0.000020

Location numbers refer to sampled areas in the experiments, as shown in Fig. 5.

crystallites), melt (preserved as glass), and an exsolved volatile phase (predominantly  $\text{CO}_2$  preserved as vesicles). It should be noted that adding  $\text{CO}_2$  to the system causes a significant drop in  $\text{H}_2\text{O}$  solubility, which may allow  $\text{H}_2\text{O}$  to occupy some of the volatile phase (Botcharnikov *et al.*, 2005; and see discussion). Hydrous experiments with  $t_d \geq 90$ s are texturally the most simple of the entire experimental series, with only two phases detected: melt (a glass of varying composition) and exsolved volatiles (as bubbles).

The melt in the experimental products comprises two compositionally distinct domains that are defined with respect to their calcium content, as this is the most variable major element along with silica. There exists (1) a Ca-normal (or ‘Merapi-like’) end-member, with a CaO content in the range 7.98–9.99 wt % (compare anhydrous M-94-a-107 with CaO wt % = 8.89 with hydrous M-94-a-107 with CaO wt % = 9.19), and (2) a Ca-enriched (‘contaminated’) end-member, with a CaO content up to *c.* 36 wt %. A diffuse, hybrid composition melt zone exists where the Ca-normal and Ca-rich melts are in contact.

### Interfaces in the experiments

Carbonate is always bordered by a zone of Ca-enriched glass, which can be distinguished in the BSE images by its brighter appearance, in strong contrast to the adjacent darker, Ca-normal glass. This Ca-rich border zone extends around the carbonate to varying degrees, and is most extensive in hydrous experiments (Fig. 3f and g). The contacts between the border zone and the surrounding Ca-normal glass ( $\pm$  crystals) are usually lobate to irregular in shape (Fig. 3). Calcite quench crystals are observed within the Ca-rich border zone for the shorter duration experiments only ( $t_d=0$ s and 60s, e.g. Fig. 3f). These crystals have a dendritic to feathery morphology indicating rapid undercooling and local calcium supersaturation of the experimental melts.

The contact between the two distinct glass domains (the 'glass interfacial zone', shaded grey in Fig. 4) is a chemically diffuse zone of variable extent, composed of a hybrid melt composition falling between the Ca-normal and Ca-rich glass end-members (Table 3). This glass interfacial zone is defined principally by the coupled change in the CaO and SiO<sub>2</sub> contents and is always characterized by progressive calcium enrichment and simultaneous silica depletion towards the Ca-rich glass and/or the carbonate (where present). Aluminium is strongly correlated with Si in the experimental products, with the shape of the Al profiles consistently mimicking the Si profiles (Fig. 4a–c). The profile shapes of the alkali elements Na<sub>2</sub>O, K<sub>2</sub>O and MgO differ slightly from those of SiO<sub>2</sub>, CaO, and Al<sub>2</sub>O<sub>3</sub>, probably because of the much higher diffusivities of the alkalis (e.g. Freda & Baker, 1998). The Ca-rich glass is generally characterized by depletion in alkalis, with respect to the M-94-a-107 starting composition. With the exception of peculiar behaviour at  $t_d=0$ s, the behaviour of K<sub>2</sub>O and Na<sub>2</sub>O appears to be closely coupled to that of SiO<sub>2</sub> (Fig. 4d–f). The glass interfacial zone is also characterized by a mixed <sup>87</sup>Sr/<sup>86</sup>Sr signature between the melt end-members and lies within the <sup>87</sup>Sr/<sup>86</sup>Sr range of Merapi feldspar Sr isotope values (Chadwick *et al.*, 2007; Figs 5 and 6).

The length of the glass interface along the EMPA profiles is measured as the mixing distance between end-members from the point where the glass composition begins to deviate from Ca-enriched to where it returns to the starting composition. Its length is greatest in the longest dwell time experiments, at *c.* 450  $\mu$ m, compared with only *c.* 80  $\mu$ m in the 0s experiments, demonstrating a greater degree of mixing in the longer experiments. A simple binary mixing model for the long dwell time experiment (300s) demonstrates a slight enrichment in CaO as the Ca-normal glass domain is approached, which exceeds that expected for simple chemical mixing between the end-members (Fig. 7, and see Discussion).

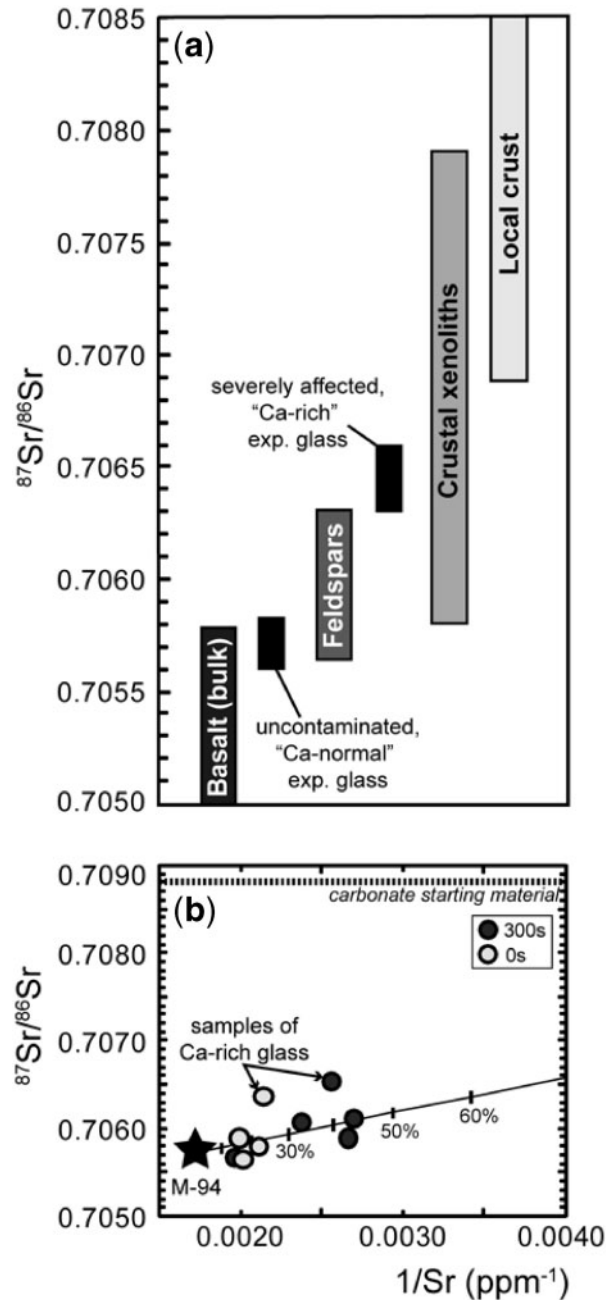


**Fig. 6.** (a) <sup>87</sup>Sr/<sup>86</sup>Sr values for Merapi basalts, feldspars, crustal xenoliths, and local crust, [compiled using data from Gertisser & Keller (2003) and Chadwick *et al.* (2007)] relative to the experimental glass (this study). It should be noted that the uncontaminated glass is within the range of recent Merapi basalts, whereas, in contrast, the Ca-enriched glass is displaced towards crustal values. (b) <sup>87</sup>Sr/<sup>86</sup>Sr binary mixing model between the end-members used in the experiments (the mixing line is straight because 1/Sr is used). The composition of the drilled samples of experimental glass has been affected by between 10 and 45% limestone-derived Sr. It should be noted that the longer dwell time experiment (300s) exhibits the greatest degree of mixing (45%). Samples from the most severely contaminated regions in both experiments (drill areas 3 in Fig. 5) are displaced from the mixing line (labelled 'samples of Ca-rich glass' on the plot). (See also Fig. 7)

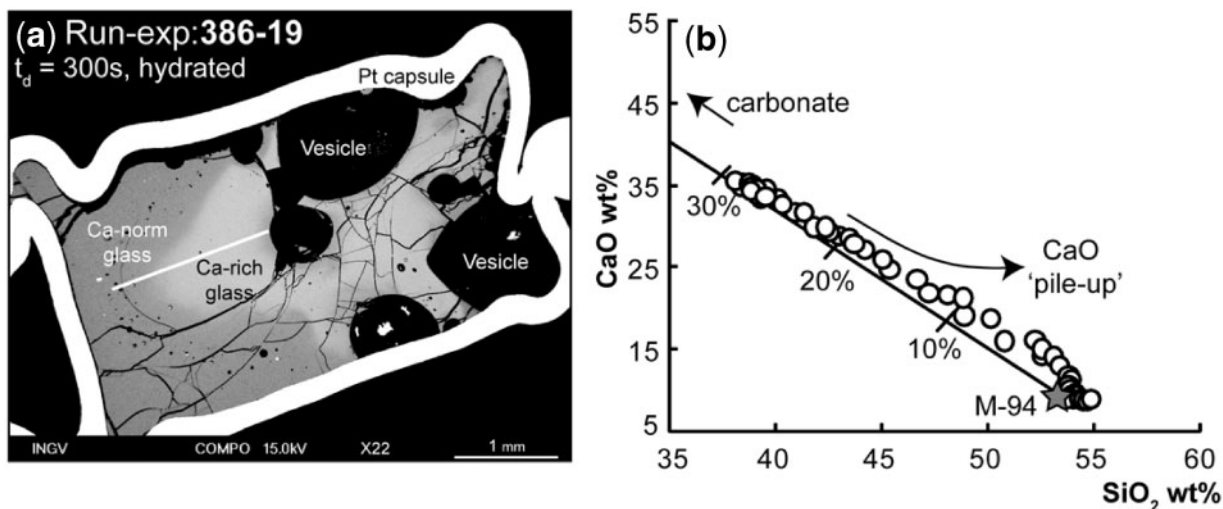


**Fig. 7.** Experiment 386-19 with microprobe analysis traverse through the intra-glass interface shown by a thick white line (a). All points from this traverse ( $n = 59$ ) are normalized to 100% and plotted on a binary mixing line between the starting compositions used in the experiments, also normalized to 100% (b). It should be noted that in the low  $\text{SiO}_2$  range, the data closely fit the mixing line, whereas towards the Ca-normal glass composition the data indicate slight CaO enrichment. This feature is interpreted as a pile-up of Ca at the Ca-normal glass interface (see discussion).

### Inter-carbonate glass

In experiments where carbonate is still found, the Ca-rich glass frequently forms pools and fracture infills within the carbonate cube. Fractures can be extremely small and thread-like, and frequently terminate in a triple-junction-type of arrangement; they are better developed in hydrous experiments than in the anhydrous ones. An excellent example of an experiment displaying these features is shown in Fig. 8, where the fractures can be seen to form a zigzag interlocked array within the carbonate, with glass-filled pools sited at the meeting point of some of these fractures. The composition of the glass within the carbonate is the same as that of the Ca-enriched glass domain that surrounds the carbonate, indicating that the inter-carbonate glass is a mixture of infiltrating silicate melt and dissolved carbonate rather than a pure *in situ* carbonate melt. Representative analyses of the inter-carbonate glass are given in Table 3.

### Vesicle distribution

Carbon dioxide vesicles are present in all experiments. The quantity, size, and distribution of the vesicles vary, however, throughout the experimental series. Multiple vesicle populations are identified in many of the experiments, in particular those in which carbonate is found, surrounded by a characteristic Ca-rich melt border. In these cases, the largest vesicles (up to 700  $\mu\text{m}$  across) are always found within the Ca-rich glass domain (Fig. 3a–d). This zone also frequently hosts a micro-bubble front at its furthest margin from the carbonate and at the carbonate–glass

contact (Fig. 8c; three generations of vesicles can be observed). In experiments where the carbonate can no longer be found, the largest bubbles are consistently found within the Ca-enriched glass domain. The maximum vesicle size measured for this experimental series is 1.39 mm in a hydrous experiment of 300s duration (Figs 3j and 9), suggesting that bubbles tend to coalesce with increasing experimental run-time. Overall vesicle distribution patterns are similar in both the anhydrous and hydrous series but vesicle density is greater in the hydrous series (see Misiti *et al.*, 2008). In comparison, vesiculation is much more vigorous in the carbonated experiments than in the corresponding control experiments in which no carbonate was added. In the hydrous control experiment(s) vesicles are randomly distributed and vesicle size is more or less constant at about 1  $\mu\text{m}$ , whereas relatively large vesicles up to 197  $\mu\text{m}$  across can be found within the Ca-contaminated glass where limestone has been added to the capsule. The 1  $\mu\text{m}$  vesicles observed in the control experiments can also be found in the ‘unaffected’ regions in the decarbonation experiments and probably simply represent ‘shrinkage bubbles’.

### Testing for pressure effects: 1 GPa experiment

Although we could not test the effect of lowering the pressure to <0.5 GPa on the experimental system, we performed a 300s hydrated experiment at 1 GPa to test the influence of increasing the pressure. The result of this experiment is shown in the BSE image in Fig. 9, alongside a 0.5 GPa equivalent experiment for direct

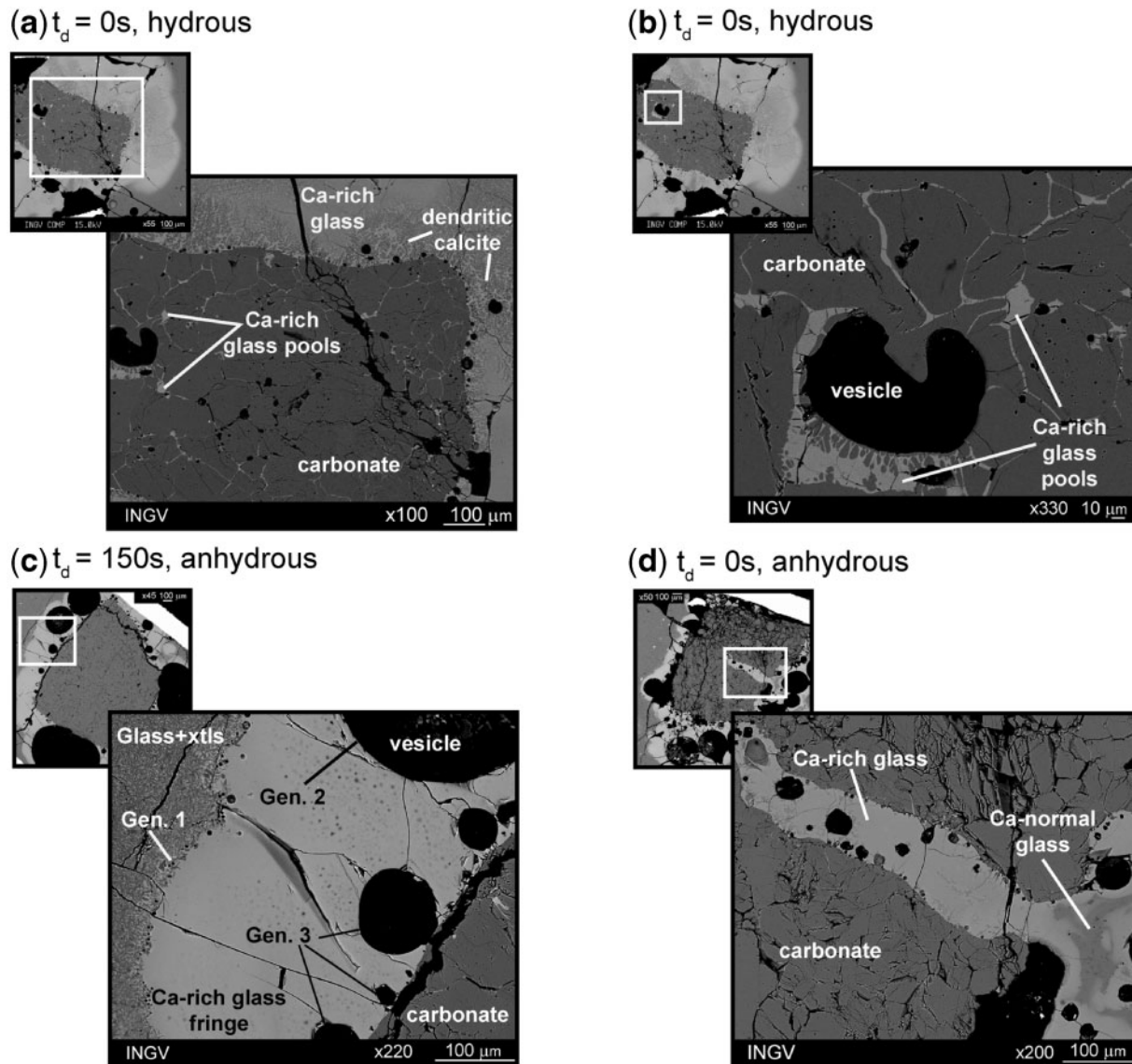


**Fig. 8.** Fine-scale textural features of experimental products. (a) An overview of the intra-carbonate glass with Ca-rich glass forming a fine network of fracture in-fill and locally collecting in pools. Dendritic calcite crystals are also visible within the Ca-rich glass. (b) At higher magnification, intra-carbonate glass can be seen to collect into pools and the nature of the termination points of the intra-carbonate veinlets is visible. (c) Three generations of vesicles extending from the carbonate grain are shown, labelled Gen. 1, 2, and 3. (d) Ca-normal glass (dark grey) displays a 'swirly', mingled texture within the Ca-enriched glass (light grey).

comparison. The 1 GPa experiment is texturally similar to the 0.5 GPa experiment, and the vesicles produced are similarly sized.

### NATURAL MERAPI CALC-SILICATE XENOLITHS

To complement our experimental data, we made detailed observations on two selected and representative calc-silicate xenoliths hosted within Merapi basaltic-andesite.

Sample MXCS-0 (cut into seven sections, a–g) and sample MXCS-1 (cut into two sections, a and b) are shown at hand-specimen scale in Fig. 2. These xenoliths have previously been described in terms of their mineralogy, whole-rock geochemistry, and their major element and Sr isotope variation in single plagioclase crystals by Chadwick *et al.* (2007, and references therein). Representative major element analyses of mineral and glass phases are given in Table 5 and notable micro-textural features of the xenoliths are illustrated in Fig. 10.

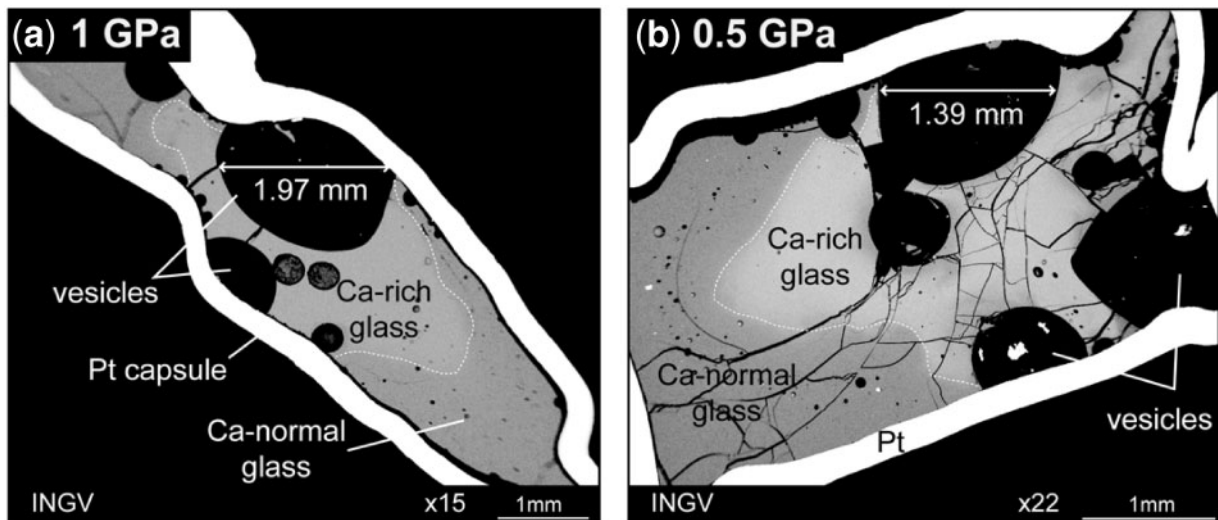


**Fig. 9.** Comparison of an experimental run at  $P=1$  GPa (a) with a similar run at 0.5 GPa (b), also shown in (Fig. 3j). Both experiments were run at  $T=1200^{\circ}\text{C}$ ,  $t_d=300\text{s}$ , using hydrous starting material, and display the same major textural features. The carbonate has assimilated and given rise to two compositionally distinct domains of glass (the boundary between the two domains of glass is highlighted with white dashed lines for clarity). The sizes of the vesicles in these experiments are the maximum for all experiments reported in this study, and are confined to the Ca-enriched glass zones. It should be noted that although the vesicles are larger in the 1 GPa experiment, they are also fewer, which indicates a greater degree of bubble coalescence in this experiment.

The xenoliths comprise a skarn-type mineral assemblage, dominated by crystallization of wollastonite and anorthite (up to  $\text{An}_{98}$ ). Also present are diopside, quartz, apatite, titanite, Fe-oxides, calcite, and minor amounts of other calcium-silicate minerals such as grossular garnet, tremolite, larnite, and spurrite. Examination of the xenoliths with the scanning electron microscope (i.e. on the micron-scale) reveals features that have counterparts in the experimental system.

Vesicular textures are very common within the xenoliths, and are best developed along magma–xenolith contact zones at the hand-specimen scale (Fig. 2). On a finer scale, we observe micro-vesiculation throughout the samples, lending a sponge-like appearance to the most densely vesiculated zones (Fig. 10a and b). Although the xenoliths are thermally metamorphosed and largely recrystallized, small amounts of  $\text{CaCO}_3$  are still preserved in places. Calcium carbonate is also found as inclusions within wollastonite crystals (Fig. 10c). Carbonate can be found bordered by a Ca-rich ('hyper-calcic') glassy zone with the composition of spurrite, which is in turn closely associated with larnite (Fig. 10b). Ca-enriched glassy regions can also be found forming part of a compositional gradient between wollastonite and nearby larnite (Fig. 10a and c).

## DISCUSSION

The following discussion focuses on mechanisms of carbonate assimilation and the implications of our experimental results for the magmatic system at Merapi volcano, including both deep and shallow-level parts of the system.

Much of the discussion focuses on the hydrated experiments, as these are considered a more reliable representation of the actual compositions involved in carbonate assimilation by a moderately hydrous basaltic-andesitic magma in nature.

### Mechanisms and timescale of carbonate assimilation

The principal process of carbonate assimilation observed in the experiments is carbonate dissociation; that is, the breakdown of the  $\text{CaCO}_3$  molecule into its component parts  $\text{CaO}$  and  $\text{CO}_2$ . Transport of the resultant molecules in the experimental charges is governed by diffusion in response to the strong chemical gradient generated by the proximally dissociating carbonate. Carbonate dissociation and the resultant loss of  $\text{CO}_2$  are probably the main controlling factors on assimilation rates and are seen to act extremely rapidly. We can semi-quantitatively constrain the timescale of assimilation in the hydrous experiments. Two assumptions have to be made concerning the onset and the termination of assimilation. (1) Inspection of Fig. 3f demonstrates that carbonate dissociation began before the target temperature of  $1200^{\circ}\text{C}$  was reached. We hence estimate the onset of carbonate assimilation at  $t_d < -60\text{s}$ , based on the rapid rate of carbonate assimilation from  $t_d=0\text{s}$  to  $t_d=60\text{s}$ . (2) Carbonate assimilation apparently ceased by  $t_d=90\text{s}$ . However, in preparation for micro-milling, the experiments were polished further, and exposed a minute amount of residual carbonate deep in the experimental capsule at  $t_d=300\text{s}$ . We none the less set

Table 5: Representative EMP analyses of minerals and glass in Merapi xenoliths

Phase:	Larnite	Spurrite	Glass border at Wo			Calcite	
Sample:	MXCS-c	MXCS-g	MXCS-c	MXCS-g	MXCS-g	MXCS-a	MXCS-g
<i>wt %</i>							
SiO <sub>2</sub>	34.12	26.36	32.23	31.56	31.62	0.08	0.14
TiO <sub>2</sub>	0.05	0.02	0.05	0.03	0.03	0.00	0.00
Al <sub>2</sub> O <sub>3</sub>	0.07	0.08	0.00	0.07	0.05	0.01	0.25
FeO	0.09	0.04	0.04	0.00	0.07	0.02	0.05
MnO	0.00	0.00	0.01	0.00	0.06	0.01	0.19
MgO	0.01	0.00	0.02	0.00	0.01	0.01	0.04
CaO	65.97	62.71	61.57	61.44	62.08	56.81	47.55
Na <sub>2</sub> O	0.00	0.03	0.03	0.00	0.01	0.00	0.04
K <sub>2</sub> O	0.00	0.01	0.00	0.01	0.02	0.00	0.01
P <sub>2</sub> O <sub>5</sub>	0.04	0.05	0.02	0.06	0.03	0.04	0.02
Total*	100.35	89.30	93.97	93.17	93.98	56.98	48.29

Phase	Wollastonite			Pyroxene		Plag An <sub>98</sub>	Titanite
Sample	MXCS-b	MXCS-c	MXCS-g	MXCS-1A	MXCS-1B	MXCS-b	MXCS-b
<i>wt %</i>							
SiO <sub>2</sub>	50.83	50.81	50.87	51.88	50.96	43.34	32.24
TiO <sub>2</sub>	0.00	0.05	0.10	0.03	0.14	0.12	38.25
Al <sub>2</sub> O <sub>3</sub>	0.24	0.05	0.08	0.44	0.80	35.52	1.41
FeO	0.63	0.47	0.84	14.85	16.84	0.29	0.73
MnO	0.40	0.41	0.61	0.40	0.81	0.01	0.11
MgO	0.14	0.14	0.14	8.51	6.66	0.00	0.00
CaO	47.71	47.78	47.84	23.86	23.80	20.21	27.58
Na <sub>2</sub> O	0.02	0.00	0.03	0.07	0.16	0.18	0.00
K <sub>2</sub> O	0.00	0.01	0.01	0.01	0.05	0.01	0.00
P <sub>2</sub> O <sub>5</sub>	0.05	0.00	0.01	0.03	0.00	0.06	0.22
Total	100.02	99.72	100.53	100.08	100.22	99.74	100.54

\*Analysis totals for the glassy border zones in the xenoliths are low (<95 wt %) as a result of dissolved volatiles. Calcite and spurrite totals are low because of their CO<sub>2</sub> component.

$t_d = 300$ s as the time required for assimilation of the limestone cube, assuming that the minute amount of residual carbonate will not affect our timescale beyond an error of a few seconds. Bearing these points in mind, assimilation of 9.75 mg limestone (average) in 41.93 mg of magma (average) requires probably not more than *c.* 330s in total, under these experimental conditions. It should be noted that the Ca-rich glass remains in contact with the carbonate throughout the experiment, and becomes saturated in the dissolving components, which then give rise to the calcite crystallites found in the Ca-rich zone in some cases. This indicates that carbonate assimilation is to some extent limited by the diffusivity of Ca through the

contaminated melt region. In nature, we would expect convection within the melt to remove the Ca-rich glass from the carbonate reaction interface (c.f. Seedhouse & Donaldson, 1996), which would increase the rate of assimilation by maintaining a large compositional gradient at the boundary between the carbonate and the host melt.

*In situ* melting of the solid carbonate was not identified in the experiments presented here. Intra-carbonate glass, occurring as pools and along fractures within the limestone cube, is calcium silicate in composition, indicating that it formed as a result of a mixture of the carbonate components and the M-94-a-107 silicate melt (i.e. a solution of carbonate in the melt; see Table 4 for composition).

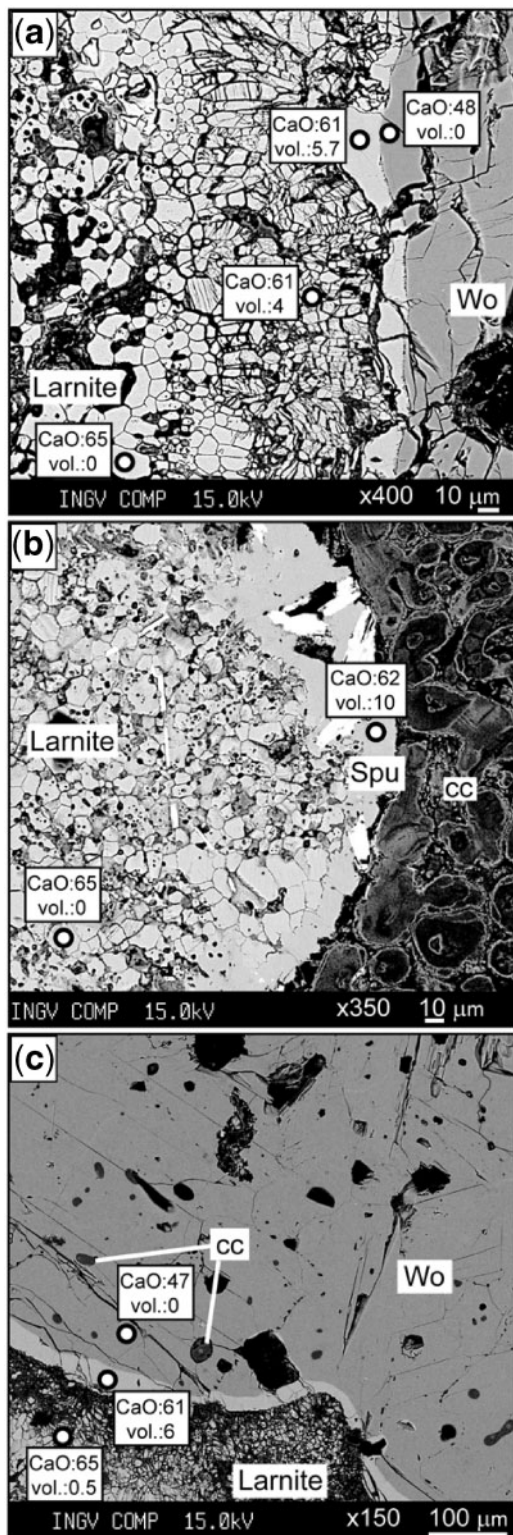


**Fig. 10.** Selected BSE images displaying textural features within a representative set of natural Merapi calc-silicate xenoliths. cc, calcium carbonate; Wo, wollastonite; Spu, spurrite; vol, volatiles. (a) Sample MXCS-0-c contains larnite with a pervasive micro-vesicular texture that grades into a slightly less calcic glassy zone towards wollastonite.

Interestingly, the glass-filled fractures frequently intersect in a triple-junction arrangement (Fig. 8a and b), which could indicate grain-boundary melting. Based on the composition of the melt, we suggest that the network of intra-carbonate glass represents infiltrating Ca-enriched M-94-a-107 melt intruding the disaggregating and dissociating carbonate, which has a polygonal fracture pattern and a set of original mineral cleavages that allow the rapid advance of invading melt. Pure calcium carbonate melts at temperatures in excess of 1300°C at 0.5 GPa (Irving & Wyllie, 1975). However, under magmatic conditions, calcite is prone to dissociation before its melting temperature is reached. We know that this process must begin before the target temperature of 1200°C is reached (i.e. during the experiment at heat-up phase) as is evidenced by the presence of a Ca-rich melt at  $t_d=0$ s. Calcite begins to dissociate at around 600°C at atmospheric pressure (e.g. Ar & Doğu, 2001); however, the temperature at which this process begins increases with elevated CO<sub>2</sub> pressure (Stern & Weise, 1969). Pressurizing our experiments to 0.5 GPa is probably the reason why some carbonate remains undissolved in the zero-time experiments, even though they were heated to 1200°C. However, we see that once the carbonate is no longer thermally stable it dissociates extremely rapidly, particularly in the hydrated runs.

Carbonate assimilation results in the generation of compositionally distinct melt domains with strongly contrasting viscosities. We can calculate the melt viscosities using the model of Giordano *et al.* (2008), with  $T$  set at 1200°C. The model does not incorporate a pressure component, but this should not affect the viscosity calculations significantly, given that melt viscosity is only weakly dependent on pressure (Richet & Bottinga, 1995). In addition, the model is not calibrated to calculate viscosities for melts with CaO contents exceeding 26 wt %. For this reason we cannot reliably estimate the viscosity of the most Ca-enriched experimental melts (with CaO in excess of, for example, 34 wt %), but we can use melt compositions from the glass interfacial zone, which are moderately enriched in CaO (up to 24 wt %) and which will provide some insights into the rheological properties of the contaminated melts. We focus on the hydrous melt composition, and calculate  $\log \eta = 1.37$  Pa s for a composition representative of the Ca-normal melt (experiment 386-19, CaO = 9.75 wt %, Table 3) and  $\log \eta = 0.27$  Pa s for a composition representative of a moderately Ca-enriched melt (experiment 376-11, CaO = 24 wt %, Table 3).

(b) Sample MXCS-0-g contains preserved carbonate bordered by glass with the composition of spurrite, which, in turn, is bordered by larnite. (c) Sample MXCS-0-g contains carbonate inclusions hosted in wollastonite. Similar to (a), a Ca-gradation exists between the larnite and wollastonite. Numbers in (a)–(c) are CaO wt % and volatiles present wt %. (See Table 5 for representative analyses of minerals and glass in the xenoliths.)

The moderately Ca-enriched melt has a very low viscosity relative to the dataset of silicate melt viscosities used to calibrate the model of Giordano *et al.* (2008). This may not be too surprising, considering that carbonatite melts are among the lowest viscosity melts on Earth (Dobson *et al.*, 1996). For example, a K<sub>2</sub>Ca(CO<sub>3</sub>)<sub>2</sub> melt at 1200°C has  $\log \eta \approx -4$  Pa s [see the extrapolated trend in fig. 5 of Dobson *et al.* (1996)]. It should be noted that the CO<sub>2</sub> content of the experimental melts is not taken into account when calculating viscosity because (1) it is not incorporated in the Giordano *et al.* (2008) model and (2) it has not been measured in our experimental melts. As the effect of dissolved CO<sub>2</sub> on silicate melt viscosity is qualitatively similar to that of H<sub>2</sub>O (Bourgue & Richet, 2001), we expect that the experimental melts will, in fact, be less viscous than the calculations suggest. In either case, the relatively low viscosity of the Ca-rich melt has implications for some geochemical features of the experiments. For instance, the CaO ‘pile-up’ at the glass interfaces (Fig. 7) may be a function of contrasting melt viscosities, with CaO accumulating where it reaches a rheological barrier (the Ca-normal glass) that inhibits or slows diffusion. The extent of the contaminated glass is, in turn, dependent on the rate of, for example, Ca (and also Sr) diffusion away from the carbonate and its ability to overcome this barrier. What we see in the experimental products is a ‘frozen-in’ CaO (and Sr) pile-up effect against such a rheological boundary.

The duration of the experiments is too short for complete homogenization of the melts to occur. We observe the onset of physical magma mixing (mingling) in localized regions of the experimental charge (e.g. Fig. 8d), probably as a consequence of the differencing melt viscosities and/or compositional convection. Widely contrasting viscosities between melts can hinder the chemical mixing process (e.g. Watson & Jurewicz, 1984; Grasset & Albarède, 1994; Poli *et al.*, 1996; Troll *et al.*, 2004), which would explain the mingled melt domains over distances of up to *c.* 100 µm in the experiments. Minor amounts of compositional convection (e.g. Seedhouse & Donaldson, 1996) may also give rise to the mingled textures and may be an additional mechanism of mass transport. The major interactive process between the melts, however, is chemical mixing by interdiffusion. This is evidenced by diffuse mixing zones between the melts over a range of distances from *c.* 80 to 450 µm (Fig. 4). Given sufficient time, the melts will mix fully, despite their contrasting viscosities. This is supported by plotting the composition of the CaO-rich melt in the ternary system (Na<sub>2</sub>O)–(Al<sub>2</sub>O<sub>3</sub> + SiO<sub>2</sub>)–(CaO) (Lee & Wyllie, 1998), where it falls outside the miscibility gap. The efficacy of mixing is hence time-dependent in the experiments, with mixing zones at their widest in the long dwell time experiments (i.e. *c.* 450 µm wide at 300s vs *c.* 80 µm wide at 0s; Fig. 4).

Mixing is also reflected in the Sr isotope systematics of the melts. The <sup>87</sup>Sr/<sup>86</sup>Sr profiles fit the CaO profiles well (Fig. 5), hence they are well correlated with the major index of contamination in the experiments (i.e. CaO). When placed in a regional context, the contaminated experimental glass overlaps the upper <sup>87</sup>Sr/<sup>86</sup>Sr range for Merapi feldspars and is displaced from the Merapi basalt range towards crustal values (Fig. 6). This supports a carbonate assimilation origin for the radiogenic, crustally contaminated zones in Merapi feldspars. When plotted on a binary mixing line (Fig. 6b), the Sr isotopes exhibit a similar feature to that shown in Fig. 7 (Ca pile-up plot), with the most contaminated samples deviating from the mixing line. Furthermore, the longer dwell time experiment demonstrates a greater degree of mixing than the short dwell time experiment. This is consistent with the observations made on the major element profiles, whose interfacial mixing zones increase in length with time. It can be seen from a comparison of the mixing plots (Figs 6b and 7) that the most contaminated glass in the 300s experiment is a mixture of *c.* 40–45% carbonate-derived <sup>87</sup>Sr/<sup>86</sup>Sr but only *c.* 30% carbonate-derived CaO, probably indicating somewhat different rates of transport of Ca vs Sr in the experiments.

#### *Pressure effects on the decarbonation reaction*

The experiments so far discussed were carried out at 0.5 GPa, simulating a mid- to deep crustal magma chamber. To test for pressure effects on the decarbonation reaction we carried out a hydrous experiment at *P* = 1 GPa and *t<sub>d</sub>* = 300s (Fig. 9). With respect to major textural features, the 1 GPa experiment is consistent with equivalent experiments run at 0.5 GPa. Vesicles produced at 1 GPa reach a maximum width of 197 µm, which is the same order of magnitude as the maximum vesicle width measured at 0.5 GPa of 139 µm; however, there were fewer vesicles present, explaining the slightly larger size in the 1 GPa experiment by simple coalescence. The outcomes of the 1 GPa experiment thus suggest that pressure is not a major influence on the carbonate dissociation reaction in the pressure range 0.5 GPa < *P* < 1 GPa, and that increasing the pressure in the system will cause no perceivable change in the experimental results. Pressure effects may, however, occupy a more important role in a shallower system such as the upper parts of the interconnected magmatic system beneath Merapi or in the volcanic conduit. Although we could not directly test the effect of lower pressure on the decarbonation process, we expect that CO<sub>2</sub> exsolution from the melt will be considerably more vigorous than that observed at 0.5 GPa, given that CO<sub>2</sub> solubility in silicate melts exhibits a positive pressure dependence (Sparks *et al.*, 1994, and references therein). Moreover, a basaltic magma at 0.5 GPa and 1200–1400°C can dissolve less than 1 wt % CO<sub>2</sub> (Blank & Brooker, 1994).

Decreasing the pressure in our experimental system will thus cause an additional <1 wt % CO<sub>2</sub> to exsolve from the basaltic-andesite magma. This is minor in comparison with the large amount of CO<sub>2</sub> liberated from the carbonate dissociation reaction.

Decompression experiments in which carbonate-bearing mantle xenoliths were brought from 2.5 GPa to 1.0 GPa demonstrate that carbonate dissociates rapidly on decompression, effectively liberating its CO<sub>2</sub> component (Canil, 1990). We can hence infer that in the high-level parts of the Merapi magmatic system, limestone will be unstable and the decarbonation reaction will proceed at an even higher rate than in our 0.5 GPa experiments. The increased instability of carbonate under these (shallow) conditions may drive sudden over-pressurization of the uppermost parts of the system, and furthermore, if carbonate xenoliths are carried through the conduit on eruption, the effect of decompression may severely intensify volcanic explosions.

### Implications for the deep-seated system at Merapi

#### *Contamination via a crustal melt phase*

Calcium contamination of the M-94-a-107 basaltic-andesite starting melt is a ubiquitous feature of the experimental products. Carbonate assimilation results in a Ca-enriched, desilicified, and high <sup>87</sup>Sr/<sup>86</sup>Sr melt phase that is in diffusive contact with the normal, starting-composition melt. Evidence of a calc-silicate contaminant melt in the Merapi system can be found in the calc-silicate xenoliths and the high-Ca, high <sup>87</sup>Sr/<sup>86</sup>Sr, feldspar zones. However, because the natural system is more complex than the experiments, we can expect that the occurrence of SiO<sub>2</sub> in carbonates (e.g. in 'dirty' or silicic limestones) plus a high SiO<sub>2</sub> activity in the magma will promote crystallization of calc-silicate minerals such as wollastonite, spurrite and larnite along with generation of a CO<sub>2</sub> volatile phase. Such products of carbonate assimilation are found intimately associated in the natural Merapi xenoliths studied: (1) carbonate inclusions are found in wollastonite (Fig. 10c); (2) wollastonite is found mantled by a 'hyper-calcic' glass, forming a compositional gradient between the wollastonite and nearby larnite (Fig. 10a and c); (3) carbonate is found bordered by a glass zone with the composition of spurrite, which is in turn bordered by larnite (Fig. 10b); (4) vesicles recording carbonate degassing are present throughout the xenoliths (Fig. 2). We should bear in mind that many of the xenoliths represent the 'end-products' of magma-carbonate interaction in nature (or near end-products, depending on their residence time), but they none the less contain a record that resembles our experimental products. Model mineral stability fields have been calculated using THERMOCALC (Powell & Holland, 1988). With pressure set at 0.2 GPa

(shallow system), wollastonite is the first stable phase following reaction between calcium carbonate and available silica in the presence of a CO<sub>2</sub>-bearing fluid at *c.* 600°C. With increasing temperature (and/or addition of water), spurrite followed by larnite will stabilize, also following reaction of calcium carbonate and silica, thus verifying the paragenesis inferred from the xenoliths. It should be noted that increasing the pressure in the model serves to increase the temperature at which the various phases are stable. For the deeper parts of the Merapi system, the Ca-rich melt in the experiments is hence interpreted as a precursor to the 'hyper-calcic' phases in the xenoliths (i.e. spurrite and larnite).

A consideration of all of the experimental data reinforces the above point. In Fig. 11 we see a progressive enrichment of the starting material in the limestone-derived CaO. The glass analyses plotted represent all of the time stages of carbonate assimilation studied, and demonstrate how carbonate assimilation progresses and causes the contaminant melt to evolve towards the composition of the 'hyper-calcic' contaminated regions in the calc-silicate xenoliths. This is strong evidence for the presence of continuing, progressive carbonate assimilation at Merapi volcano and for contamination via a carbonated, extremely calcic melt phase. Limestone contamination in this manner has also been suggested for other settings, such as the Hortavaer igneous complex in Norway (Barnes *et al.*, 2005), the Colli Albani volcanic district, Italy (Gaeta *et al.*, 2009), and Oldoinyo Lengai volcano, Tanzania (Mitchell, 2009).

#### *Effect of a mobile calcic melt on the magma system*

As a result of their relatively low viscosities, carbonated melts are highly mobile, thus enhancing their ability to migrate through a partially crystallized magma body and possibly even mobilize semi-arrested regions of the magma system. In the deeper parts of the Merapi system, this process could aid mixing between magma pockets (e.g. Nakagawa *et al.*, 2002) and allow recycling of phenocrysts (e.g. Charlier *et al.*, 2005). The relatively mobile Ca-rich, high <sup>87</sup>Sr/<sup>86</sup>Sr melt will then be able to contaminate local regions of the system, by convective mixing and/or diffusion.

The rheology of the melt also has implications for bubble growth over relatively short length scales. The Ca-rich melt phase gives rise to the largest bubbles, which is probably a function of its relatively low viscosity, in addition to its volatile content. This type of melt offers less resistance for bubble expansion and coalescence. Moreover, the Ca-rich zone is locally CO<sub>2</sub> supersaturated, as a result of the proximally decomposing carbonate, favouring additional bubble growth and enlargement.

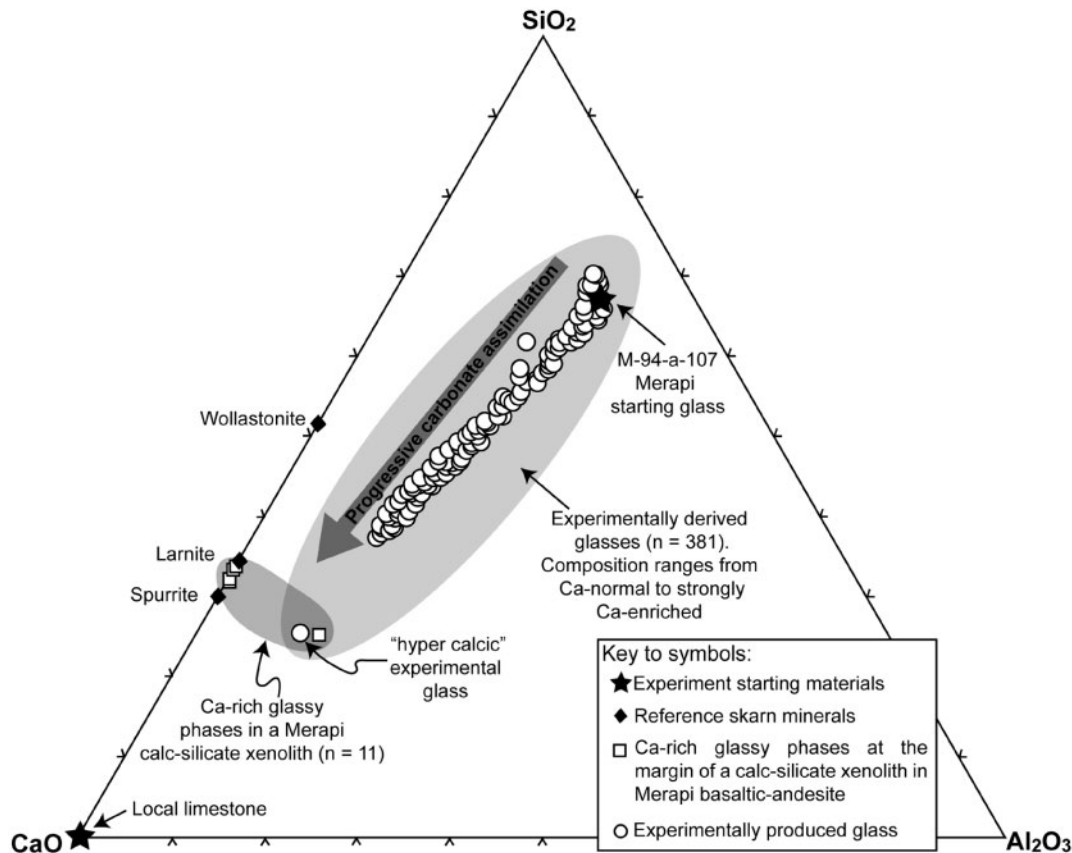


**Fig. 11.** Ternary plot (SiO<sub>2</sub>-CaO-Al<sub>2</sub>O<sub>3</sub>) displaying glass analyses representative of all the experiments in this study. Analyses of mineral and glass phases in a representative natural Merapi calc-silicate xenolith are shown for comparison. Experimental data (both anhydrous and hydrous, grey field on the plot) include: 374-4 ( $n = 23$ ), 374-5 ( $n = 4$ ), 375-6 ( $n = 11$ ), 375-7 ( $n = 5$ ), 376-10 ( $n = 32$ ), 376-11 ( $n = 35$ ), 379-16 ( $n = 11$ ), 379-17 ( $n = 32$ ), 386-18 ( $n = 45$ ), 386-19 ( $n = 81$ ), 387-20 ( $n = 41$ ), 387-21 ( $n = 61$ ). Merapi xenolith data include: MXCS-a ( $n = 4$ ), MXCS-b ( $n = 2$ ), MXCS-c ( $n = 2$ ), MXCS-g ( $n = 3$ ). It should be noted that the experimental melts range from the relatively unaffected, Ca-normal composition (similar to the M-94-a-107 basaltic-andesite starting composition) to strongly contaminated, Ca-enriched glass.

## Implications for the shallow system at Merapi

### *The volatile budget*

Volatile exsolution from the experimental melts, and associated vesiculation, reaches a maximum in the Ca-rich glass, and is observed at all time intervals of magma-carbonate interaction. Water solubility in a basalt at 1200°C and 0.5 GPa is  $c. 8.5 \text{ wt } \%$  (e.g. VolatileCalc, Newman & Lowenstern, 2002). However, adding CO<sub>2</sub> to the system through carbonate dissolution causes a significant drop in H<sub>2</sub>O melt solubility (Botcharnikov *et al.*, 2005). Hence, the vesicles in the experiments may be due to exsolution of both CO<sub>2</sub> and H<sub>2</sub>O, with CO<sub>2</sub> being the most abundant volatile. As  $c. 0.4 \text{ wt } \%$  CO<sub>2</sub> is soluble in the basaltic-andesite starting material (e.g. King & Holloway, 2002), most of the CO<sub>2</sub> added to the system through carbonate assimilation is expected to be present as an exsolved volatile phase. We can hence calculate that an average of  $c. 4.3 \text{ mg}$  of CO<sub>2</sub> is liberated in the experiments,

which occupies  $c. 7 \text{ vol. } \%$  of the experimental capsule. If we consider assimilation in nature of a limestone cube with 80 m side length,  $c. 5.6 \times 10^5$  tonnes of CO<sub>2</sub> will be produced. Given the short timescale of carbonate assimilation observed in the experiments, it is wholly conceivable that up to  $5.6 \times 10^5$  tonnes of CO<sub>2</sub> could be generated over a period of 2 weeks by carbonate assimilation alone. Limestone assimilation and associated CO<sub>2</sub> release on this scale ( $5.4 \times 10^5$  tonnes of CO<sub>2</sub> over 17 days) has been inferred for Popocatepetl volcano in Mexico based on measured excess CO<sub>2</sub> emissions (Goff *et al.*, 2001).

Models of CO<sub>2</sub> provenance and fluxes at oceanic arcs generally do not take the arc crust into account as a potential volatile source (e.g. Hilton *et al.*, 2002). For example, the proportion of the components of arc contributions to the global CO<sub>2</sub> flux has been estimated at 10–15% from the mantle wedge and 85–90% from decarbonation of subducted carbonate and carbonate-bearing sedimentary rocks (after Hilton *et al.*, 2002, and references therein).

The experiments presented here show that CO<sub>2</sub> liberated from carbonate-rich lithologies in the arc crust can constitute a significant contribution to the volatile budget at subduction zones (with *c.* 32 000 t/day of excess CO<sub>2</sub> being realistic; see Goff *et al.*, 2001). Such late-stage CO<sub>2</sub> fluxes are probably highly variable over long timescales, but, in the short term, decarbonation of limestone can produce substantial amounts of crustal CO<sub>2</sub>, and this should be considered when investigating and modelling volcanic volatile budgets.

#### *Crustal decarbonation as an eruption trigger?*

Carbon dioxide gas liberation as a result of limestone assimilation at mid- to shallow crustal depths in the Merapi magmatic system may have serious implications for the eruptive dynamics of this high-risk volcano. Intense episodes of carbonate devolatilization within the mid- to upper crust have the potential to over-pressurize the magmatic system over short timescales (hours to days), which may lead to an eruptive event with very limited forewarning. Although carbonate assimilation is probably a continuing process at Merapi, its potential to act as an eruption trigger could be magnified if external forcing, such as an earthquake, were to act on the system. A case in point is the major 2006 Yogyakarta earthquake (*M* = 6.4, Walter *et al.*, 2008), which coincided with activity at Merapi. The event was followed by an up to three-fold increase in dome growth and dome collapse activity for a period of 16 days after the earthquake (Harris & Ripepe, 2007; Walter *et al.*, 2007). We speculate that stress changes and vibration in the mid- to upper crust associated with the earthquake may have fractured the crustal limestone units underlying Merapi, resulting in vigorous release of trapped CO<sub>2</sub> and renewed crustal decarbonation as a result of an increase in limestone surface area available to react with the magma. Decomposition of CO<sub>2</sub>-bearing xenoliths in this way is a much more efficient contamination mechanism than wall-rock interaction alone (e.g. Watson *et al.*, 1982; Freda *et al.*, 2008*b*). This additional CO<sub>2</sub> release, potentially of the order of 32 000 t/day (see Goff *et al.*, 2001), would have rapidly increased the CO<sub>2</sub> pressure in the system, promoting increased eruptive activity following the 2006 earthquake. The risk of such intensified episodes of carbonate devolatilization at Merapi has serious implications for hazard mitigation, which will need to be sufficiently flexible to cope with an eruptive crisis with very little forewarning. This would also apply to other volcanic systems emplaced within carbonate crustal rocks, which may likewise be susceptible to overpressurization following vigorous reaction between magma and limestone; for example, Popocatepetl, Mexico and Vesuvius, Italy, both of which have a record of sustained explosive activity.

## SUMMARY

The time-constrained series of short duration experiments presented here provides a unique opportunity to observe the textural, chemical, and isotopic interaction between mafic magma and carbonate crustal rocks as carbonate assimilation proceeds. The major features of carbonate assimilation identified are: (1) rapid decomposition and degassing of carbonate; (2) generation of a relatively low-viscosity, calcic, high <sup>87</sup>Sr/<sup>86</sup>Sr contaminated melt; (3) local CO<sub>2</sub> volatile supersaturation and subsequent vigorous bubble growth within the affected region; (4) physical mingling between the contaminated and unaffected melt domains; (5) chemical mixing between melts.

Considering the experimental data in conjunction with the existing petrological, mineralogical, and geochemical data for Merapi (e.g. Gertisser & Keller, 2003; Chadwick *et al.*, 2007), we can verify that intra-crustal to late-stage carbonate assimilation and associated volatile degassing are significant magma-chamber processes that affect mineral composition, magma evolution, and potentially the eruptive behaviour at Merapi volcano. In light of this realization, the volatile budget at Merapi demands a re-evaluation to take into account late-stage, intra-crustal decarbonation events.

## ACKNOWLEDGEMENTS

We are grateful to L. M. Schwarzkopf for providing sample material, H. Behrens for producing the hydrated glass and for KFT analysis, S. Mollo for producing the anhydrous glass, A. Cavallo for microprobe technical assistance and support at INGV, J. Malarkey for micromilling technical support, and Chris Ottley and Geoff Nowell at Durham for assistance with elemental and isotopic analysis of the microsamples respectively. F.M.D. is grateful to S. and E. Vinciguerra for their hospitality during this work. A. Skelton, O. Spieler, J. Blundy, and J. Taddeucci are thanked for stimulating and encouraging discussion. We are grateful to C. Barnes, F. Ridolfi, and one anonymous reviewer for their thorough and thoughtful reviews, which helped to greatly improve the manuscript. We also thank M. Wilson for her prompt and careful editorial handling of the manuscript. This work was supported by the Swedish Science Foundation (Vetenskapsrådet) (621-2007-5028 to V.R.T.) and by Project FIRBMIUR 'Development of innovative technologies for the environmental protection from natural events'.

## SUPPLEMENTARY DATA

Supplementary data for this paper are available at *Journal of Petrology* online.

## REFERENCES

- Abdurachman, E. K., Bourdier, J.-L. & Voight, B. (2000). Nuées ardentes of 22 November 1994 at Merapi volcano, Java, Indonesia. *Journal of Volcanology and Geothermal Research* **100**, 345–361.

- Abratis, M., Schmincke, H.-U. & Hansteen, T. H. (2002). Composition and evolution of submarine volcanic rocks from the central and western Canary Islands. *Geologische Rundschau* **91**, 562–582.
- Annen, C. & Sparks, R. S. J. (2002). Effects of repetitive emplacement of basaltic intrusions on thermal evolution and melt generation in the crust. *Earth and Planetary Science Letters* **203**, 937–955.
- Ar, I. & Doğu, G. (2001). Calcination kinetics of high purity limestones. *Chemical Engineering Journal* **83**, 131–137.
- Barnes, C. G., Prestvik, T., Sundvoll, B. & Surratt, D. (2005). Pervasive assimilation of carbonate and silicate rocks in the Hortavaer igneous complex, north-central Norway. *Lithos* **80**, 179–199.
- Beard, J. S., Abitz, R. J. & Lofgren, G. E. (1993). Experimental melting of crustal xenoliths from Kilbourne Hole, New Mexico and implications for the contamination and genesis of magmas. *Contributions to Mineralogy and Petrology* **115**, 88–102.
- Behrens, H. (1995). Determination of water solubilities in high-viscosity silicate glasses: An experimental study on NaAlSi<sub>3</sub>O<sub>8</sub> and KAlSi<sub>3</sub>O<sub>8</sub> melts. *European Journal of Mineralogy* **7**, 905–920.
- Blank, J. G. & Brooker, R. A. (1994). Experimental studies of carbon dioxide in silicate melts: solubility, speciation, and stable carbon isotope behavior. In: Carroll, M. R. & Holloway, J. R. (eds) *Volatiles in Magmas*. *Mineralogical Society of America, Reviews in Mineralogy* **30**, 157–186.
- Botcharnikov, R., Freise, M., Holtz, F. & Behrens, H. (2005). Solubility of C–O–H mixtures in natural melts: new experimental data and application range of recent models. *Annals of Geophysics* **48**, 633–646.
- Bourgue, E. & Richet, P. (2001). The effects of dissolved CO<sub>2</sub> on the density and viscosity of silicate melts: a preliminary study. *Earth and Planetary Science Letters* **193**, 57–68.
- Camus, G., Gourgaud, A., Mossand-Berthommier, P.-C. & Vincent, P.-M. (2000). Merapi (Central Java, Indonesia): An outline of the structural and magmatological evolution, with a special emphasis to the major pyroclastic events. *Journal of Volcanology and Geothermal Research* **100**, 139–163.
- Canil, D. (1990). Experimental study bearing on the absence of carbonate in mantle-derived xenoliths. *Geology* **18**, 1011–1013.
- Chadwick, J. P. (2008). Magma crust interaction in volcanic systems: Case studies from Merapi Volcano, Indonesia, Taupo Volcanic Zone, New Zealand, and Sliève Gullion, N. Ireland: PhD thesis, Trinity College Dublin, pp. 52–181.
- Chadwick, J. P., Troll, V. R., Ginibre, C., Morgan, D., Gertisser, R., Waight, T. E. & Davidson, J. P. (2007). Carbonate assimilation at Merapi volcano, Java, Indonesia: Insights from crystal isotope stratigraphy. *Journal of Petrology* **48**, 1793–1812.
- Charbonnier, S. J. & Gertisser, R. (2008). Field observations and surface characteristics of pristine block-and-ash flow deposits from the 2006 eruption of Merapi Volcano, Java, Indonesia. *Journal of Volcanology and Geothermal Research* **177**, 971–982.
- Charlier, B. L. A., Wilson, C. J. N., Lowenstern, J. B., Blake, S., Van Calsteren, P. W. & Davidson, J. P. (2005). Magma generation at a large, hyperactive silicic volcano (Taupo, New Zealand) revealed by U–Th and U–Pb systematic in zircons. *Journal of Petrology* **46**, 3–32.
- Charlier, B. L. A., Ginibre, C., Morgan, D., Nowell, G. M., Pearson, D. G., Davidson, J. P. & Ottley, C. J. (2006). Methods for microsampling and high-precision analysis of strontium and rubidium isotopes at single crystal scale for petrological and geochronological applications. *Chemical Geology* **232**, 114–133.
- Clochiatti, R., Joron, J. L., Kerinec, F. & Treuil, M. (1982). Quelques données préliminaires sur la lave du dôme actuel du volcan Merapi (Java Indonésie) et sur ses enclaves. *Comptes Rendus de l'Académie des Sciences, Série A* **295**, 817–822.
- Curray, J. R., Shor, G. G., Raitt, R. W. & Henry, M. (1977). Seismic refraction and reflection studies of crustal structure of the Eastern Sunda and Western Banda arcs. *Journal of Geophysical Research* **82**, 2479–2489.
- Dallai, L., Freda, C. & Gaeta, M. (2004). Oxygen isotope geochemistry of pyroclastic clinopyroxene monitors carbonate contributions to Roman-type ultrapotassic magmas. *Contributions to Mineralogy and Petrology* **148**, 247–263.
- Davidson, J. P., Hora, J. M., Garrison, J. M. & Dungan, M. A. (2005). Crustal forensics in arc magmas. *Journal of Volcanology and Geothermal Research* **140**, 157–170.
- de Genevraye, P. & Samuel, L. (1972). Geology of the Kendang Zone (Central and East Java). In: *Proceedings, First Annual Convention, Indonesian Petroleum Association*, pp. 17–30.
- Del Moro, A., Fulignati, P., Marianelli, P. & Sbrana, A. (2001). Magma contamination by direct wall rock interaction: constraints from xenoliths from the walls of a carbonate-hosted magma chamber (Vesuvius 1944 eruption). *Journal of Volcanology and Geothermal Research* **112**, 15–24.
- Dobson, D. P., Jones, A. P., Rabe, R., Sekine, T., Kurita, K., Taniguchi, T., Kondo, T., Kato, T., Shimomura, O. & Urakawa, S. (1996). In-situ measurement of viscosity and density of carbonate melts at high pressure. *Earth and Planetary Science Letters* **143**, 207–215.
- Donoghue, E., Troll, V. R., Schwarzkopf, L. M., Clayton, G. & Goodhue, R. (2009). Organic block coatings in block-and-ash flow deposits at Merapi Volcano, central Java. *Geological Magazine* **146**, 113–120.
- Font, L., Davidson, J. P., Pearson, D. G., Nowell, G. M., Jerram, D. A. & Ottley, C. J. (2008). Sr and Pb isotope micro-analysis of plagioclase crystals from Skye lavas: an insight into open-system processes in a flood basalt province. *Journal of Petrology* **49**, 1449–1471.
- Freda, C. & Baker, D. R. (1998). Na–K interdiffusion in alkali feldspar melts. *Geochimica et Cosmochimica Acta* **62**, 2997–3007.
- Freda, C., Gaeta, M., Palladino, D. M. & Trigila, R. (1997). The Villa Senni Eruption (Alban Hills, central Italy): the role of H<sub>2</sub>O and CO<sub>2</sub> on the magma chamber evolution and on the eruptive scenario. *Journal of Volcanology and Geothermal Research* **78**, 103–120.
- Freda, C., Baker, D. R. & Ottolini, L. (2001). Reduction of water loss from gold–palladium capsules during piston cylinder experiments by use of pyrophyllite powder. *American Mineralogist* **86**, 234–237.
- Freda, C., Gaeta, M., Misiti, V., Mollo, S., Dolfi, D. & Scarlato, P. (2008a). Magma–carbonate interaction: An experimental study on ultrapotassic rocks from Alban Hills (Central Italy). *Lithos* **101**, 397–415.
- Freda, C., Gaeta, M., Giaccio, B., Marra, F., Palladino, D. M., Scarlato, P. & Sottili, G. (2008b). Magma–country rock interaction during large mafic explosive eruptions: evidence from Colli Albani (Central Italy). In: *Abstracts, 33rd IGC 2008 Oslo, Norway (2008)*.
- Fulignati, P., Marianelli, P., Santacroce, R. & Sbrana, A. (2004). Probing the Vesuvius magma chamber–host rock interface through xenoliths. *Geological Magazine* **141**, 417–428.
- Gaeta, M., Di Rocco, T. & Freda, C. (2009). Carbonate assimilation in open magmatic systems: the role of melt-bearing skarns and cumulate forming processes. *Journal of Petrology* **50**, 361–385.
- García-Moreno, O., Castro, A., Corretgé, L. G. & El-Hmidi, H. (2006). Dissolution of tonalitic enclaves in ascending hydrous granitic magmas: An experimental study. *Lithos* **89**, 245–258.
- Gasparon, M. & Varne, R. (1998). Crustal assimilation versus subducted sediment input in west Sunda arc volcanics: an evaluation. *Mineralogy and Petrology* **64**, 89–117.

- Gasparon, M., Hilton, D. R. & Varne, R. (1994). Crustal contamination processes traced by helium isotopes: Examples from the Sunda arc, Indonesia. *Earth and Planetary Science Letters* **126**, 15–22.
- Gertisser, R. (2001). Gunung Merapi (Java, Indonesia): Eruptionsgeschichte und magmatische Evolution eines Hochrisiko-Vulkans. PhD thesis: Universität Freiburg.
- Gertisser, R. & Keller, J. (2003). Trace elements and Sr, Nd, Pb and O isotope variations in medium-K and high-K volcanic rocks from Merapi Volcano, Central Java, Indonesia: Evidence for the involvement of subducted sediments in Sunda arc magma genesis. *Journal of Petrology* **44**, 457–489.
- Gilg, H. A., Lima, A., Somma, R., Belkin, H. E., De Vivo, B. & Ayuso, R. A. (2001). Isotope geochemistry and fluid inclusion study of skarns from Vesuvius. *Mineralogy and Petrology* **73**, 145–176.
- Giordano, D., Russell, J. K. & Dingwell, D. B. (2008). Viscosity of magmatic liquids: a model. *Earth and Planetary Science Letters* **271**, 123–134.
- Goff, F., Love, S. P., Warren, R. G., Counce, D., Obenholzner, J., Siebe, C. & Schmidt, S. C. (2001). Passive infrared remote sensing evidence for large, intermittent CO<sub>2</sub> emissions at Popocatepetl volcano, Mexico. *Chemical Geology* **177**, 133–156.
- Grasset, O. & Albarède, F. (1994). Hybridization of mingling magmas with different densities. *Earth and Planetary Science Letters* **121**, 327–332.
- Hall, R. (2002). Cenozoic geological and plate tectonic evolution of SE Asia and the SW Pacific: computer-based reconstructions, model and animations. *Journal of Asian Earth Sciences* **20**, 353–431.
- Hamilton, W. (1979). Tectonics of the Indonesian Region. *US Geological Survey, Professional Papers* **1078**, 1–345.
- Harris, A. J. L. & Ripepe, M. (2007). Regional earthquakes as a trigger for enhanced volcanic activity: evidence from MODIS thermal data. *Geophysical Research Letters* **34**, LO2304, doi:10.1029/2006GL028251.
- Hilton, D. R., Fischer, T. P. & Marty, B. (2002). Noble gases and volatile recycling at subduction zones. In: Porcelli, D. P., Ballentine, C. J. & Wieler, R. (eds) *Noble Gases. Mineralogical Society of America, Reviews in Mineralogy* **47**, 319–370.
- Huang, W.-L., Wyllie, P. J. & Nehru, C. E. (1980). Subsolidus and liquidus phase relationships in the system CaO–SiO<sub>2</sub>–CO<sub>2</sub> to 30 kbar with geological applications. *American Mineralogist* **65**, 285–301.
- Hudon, P., Baker, D. R. & Toft, P. B. (1994). A high-temperature assembly for 1.91 cm (3/4") piston-cylinder apparatus. *American Mineralogist* **79**, 145–147.
- Iacono Marziano, G., Gaillard, F. & Pichavant, M. (2008). Limestone assimilation by basaltic magmas: an experimental re-assessment and application to Italian volcanoes. *Contributions to Mineralogy and Petrology* **155**, 719–738.
- Iezzi, G., Mollo, S., Ventura, G., Cavallo, A. & Romano, C. (2008). Experimental solidification of anhydrous latitic and trachytic melts at different cooling rates: The role of nucleation kinetics. *Chemical Geology* **253**, 91–101.
- Irving, A. J. & Wyllie, P. J. (1975). Subsolidus and melting relationships for calcite, magnesite and the join CaCO<sub>3</sub>–MgCO<sub>3</sub> to 36 kb. *Geochimica et Cosmochimica Acta* **39**, 35–53.
- Johnston, A. D. & Wyllie, P. J. (1988). Interaction of granitic and basic magmas: experimental observations on contamination processes at 10 kbar with H<sub>2</sub>O. *Contributions to Mineralogy and Petrology* **98**, 352–362.
- King, P. L. & Holloway, J. R. (2002). CO<sub>2</sub> solubility and speciation in intermediate (andesitic) melts: The role of H<sub>2</sub>O and composition. *Geochimica et Cosmochimica Acta* **66**, 1627–1640.
- Knesel, K. M. & Davidson, J. P. (2002). Insights into collisional magmatism from isotopic fingerprints of melting reactions. *Science* **296**, 2206–2208.
- Koulakov, I., Bohm, M., Asch, G., Lühr, B.-G., Manzanares, A., Brotopuspito, K. S., Fauzi, P., Purbawinata, M. A., Puspito, N. T., Ratdomopurbo, A., Kopp, H., Rabbel, W. & Sheygunova, E. (2007). P and S velocity structure of the crust and the upper mantle beneath central Java from local tomography inversion. *Journal of Geophysical Research* **112**, B08310, doi:10.1029/2006JB004712.
- Lee, W.-J. & Wyllie, P. J. (1998). Petrogenesis of carbonatite magmas from mantle to crust, constrained by the system CaO–(MgO + FeO)–(Na<sub>2</sub>O + K<sub>2</sub>O)–(SiO<sub>2</sub> + Al<sub>2</sub>O<sub>3</sub> + TiO<sub>2</sub>)–CO<sub>2</sub>. *Journal of Petrology* **39**, 495–517.
- Macdonald, R., Hawkesworth, C. J. & Heath, E. (2000). The Lesser Antilles volcanic chain: a study in arc magmatism. *Earth-Science Reviews* **49**, 1–76.
- Macpherson, C. G., Gamble, J. A. & Matthey, D. P. (1998). Oxygen isotope geochemistry of lavas from an oceanic to continental arc transition, Kermadec–Hikurangi margin, SW Pacific. *Earth and Planetary Science Letters* **160**, 609–621.
- McLeod, P. & Sparks, S. J. (1998). The dynamics of xenoliths assimilation. *Contributions to Mineralogy and Petrology* **132**, 21–33.
- Médard, E., McCammon, C. A., Barr, J. A. & Grove, T. L. (2008). Oxygen fugacity, temperature reproducibility, and H<sub>2</sub>O contents of nominally anhydrous piston-cylinder experiments using graphite capsules. *American Mineralogist* **93**, 1838–1844.
- Misiti, V., Taddeucci, J., Freda, C., Deegan, F., Troll, V. & Blythe, L. (2008). Vesiculation of andesitic melts during carbonate assimilation. In: *Abstracts, 12th International Conference on Experimental Mineralogy, Petrology and Geochemistry (EMPG-XII), Innsbruck, Austria (2008)*.
- Mitchell, R. H. (2009). Peralkaline nepheline–natrocarbonatite immiscibility and carbonate assimilation at Oldoinyo Lengai, Tanzania. *Contributions to Mineralogy and Petrology* **158**, 589–598.
- Mollo, S., Gaeta, M., Freda, C. & Di Rocco, T. (2010). Carbonate assimilation in magmas: A reappraisal based on experimental petrology. *Lithos* **114**, 503–514.
- Nakagawa, M., Wada, K. & Wood, P. (2002). Mixed magmas, mush chambers and eruption triggers: evidence from zoned clinopyroxene phenocrysts in andesitic scoria from the 1995 eruptions of Ruapehu volcano, New Zealand. *Journal of Petrology* **43**, 2279–2303.
- Newman, S. & Lowenstern, J. B. (2002). VolatileCalc: a silicate melt–H<sub>2</sub>O–CO<sub>2</sub> solution model written in Visual Basic for excel. *Computers and Geosciences* **28**, 597–604.
- Poli, G., Tommasini, S. & Halliday, A. N. (1996). Trace element and isotopic exchange during acid–basic magma interaction processes. *Transactions of the Royal Society of Edinburgh: Earth Sciences* **87**, 225–232.
- Powell, R. & Holland, T. J. B. (1988). An internally consistent thermodynamic dataset with uncertainties and correlations: 3. Application to geobarometry, worked examples and a computer program. *Journal of Metamorphic Petrology* **6**, 173–204.
- Richet, P. & Bottinga, Y. (1995). Rheology and configurational entropy of silicate melts. In: Stebbins, J. F., McMillan, P. F. & Dingwell, D. B. (eds) *Structure, Dynamics and Properties of Silicate Melts. Mineralogical Society of America, Reviews in Mineralogy and Geochemistry* **32**, 67–93.
- Sachs, P. M. & Strange, S. (1993). Fast assimilation of xenoliths in magmas. *Journal of Geophysical Research* **98**, 19741–19754.
- Schaaf, P., Stimac, J., Siebe, C. & Macias, J. L. (2005). Geochemical evidence for mantle origin and crustal processes in volcanic rocks from Popocatepetl and surrounding monogenetic volcanoes, Central Mexico. *Journal of Petrology* **46**, 1243–1282.

- Schwarzkopf, L. M., Schmincke, H.-U. & Troll, V. R. (2001). Pseudotachylite on impact marks of block surfaces in block-and-ash flows at Merapi volcano, Central Java, Indonesia. *Geologische Rundschau* **90**, 769–775.
- Schwarzkopf, L. M., Schmincke, H.-U. & Cronin, S. J. (2005). A conceptual model for block-and-ash flow basal avalanche transport and deposition, based on deposit architecture of 1998 and 1994 Merapi flows. *Journal of Volcanology and Geothermal Research* **139**, 117–134.
- Seedhouse, J. K. & Donaldson, C. H. (1996). Compositional convection caused by olivine crystallization in a synthetic basalt melt. *Mineralogical Magazine* **60**, 115–130.
- Smith, I. E. M., Worthington, T. J., Price, R. C., Stewart, R. B. & Maas, R. (2006). Petrogenesis of dacite in an oceanic subduction environment: Raoul Island, Kermadec arc. *Journal of Volcanology and Geothermal Research* **156**, 252–265.
- Smith, T. E., Thirlwall, M. F. & Macpherson, C. (1996). Trace element and isotopic geochemistry of the volcanic rocks of Bequia, Grenadine Islands, lesser Antilles Arc: a study of subduction enrichment and intra-crustal contamination. *Journal of Petrology* **37**, 117–143.
- Smyth, H. R., Hall, R., Hamilton, J. & Kinny, P. (2005). East Java: Cenozoic basins, volcanoes and ancient basement. In: *Proceedings, Indonesian Petroleum Association, Thirtieth Annual Convention & Exhibition*.
- Smyth, H. R., Hamilton, P. J., Hall, R. & Kinny, P. D. (2007). The deep crust beneath island arcs: Inherited zircons reveal a Gondwana continental fragment beneath East Java, Indonesia. *Earth and Planetary Science Letters* **258**, 269–282.
- Sparks, R. S. J., Barclay, J., Jaupart, H. M. & Philips, J. C. (1994). Physical aspects of magma degassing I: Experimental and theoretical constraints on vesiculation. In: Carroll, M. R. & Holloway, J. R. (eds) *Volatiles in Magmas, Mineralogical Society of America, Reviews in Mineralogy* **30**, 413–445.
- Stern, K. H. & Weise, E. L. (1969). High temperature properties and decomposition of inorganic salts. Part 2: Carbonates. *National Standard Reference Data System, National Bureau of Standards (U.S.)* **30**, 32 p.
- Troll, V. R., Schwarzkopf, L. M., Gertisser, R., Buckley, C., Chadwick, J., Zimmer, M. & Sulistiyo, Y. (2003). Shallow-level processes and their impact on the eruptive behaviour in arc volcanoes: evidence from recent Merapi lavas. In: *Abstracts, State of the Arc Meeting, Portland, Oregon (2003)*.
- Troll, V. R., Donaldson, C. H. & Emeleus, C. H. (2004). Pre-eruptive magma mixing in ash-flow deposits of the Tertiary Rum Igneous Centre, Scotland. *Contributions to Mineralogy and Petrology* **147**, 722–739.
- Untung, M. & Sato, Y. (1978). *Gravity and Geological studies in Java, Indonesia. Geological Survey of Indonesia and Geological Survey of Japan, Special Publication* **6**, 207 p.
- van Bemmelen, R. W. (1949). *The Geology of Indonesia, IA, General Geology*. The Hague: Government Printing Office.
- Voight, B., Constantine, E. K., Siswamidjono, S. & Torley, R. (2000). Historical eruptions of Merapi volcano, Central Java, Indonesia, 1768–1998. *Journal of Volcanology and Geothermal Research* **100**, 69–138.
- Wagner, D., Koulakov, I., Rabbel, W., Luehr, B.-G., Wittwer, A., Kopp, H., Bohm, M. & Asch, G. & the MERAMEX Scientists (2007). Joint inversion of active and passive seismic data in Central Java. *Geophysical Journal International* **170**, 923–932.
- Walter, T. R., Wang, R., Zimmer, M., Grosser, H., Lühr, B. & Ratdomopurbo, A. (2007). Volcanic activity influenced by tectonic earthquakes: static and dynamic stress triggering at Mt. Merapi. *Geophysical Research Letters* **34**, L05304, doi:10.1029/2006GL028710.
- Walter, T. R., Wang, R., Luehr, B.-G., Wassermann, J., Behr, Y., Parolai, S., Anggraini, A., Günther, E., Sobiesiak, M., Grosser, H., Wetzel, H.-U., Milkereit, C., Sri Brotopusito, P. J. K., Harjadi, P. & Zschau, J. (2008). The 26 May 2006 magnitude 6.4 Yogyakarta earthquake south of Mt. Merapi volcano: Did lahar deposits amplify ground shaking and thus lead to the disaster? *Geochemistry, Geophysics, Geosystems* **9**, doi:10.1029/2007GC001810.
- Watson, E. B. (1982). Basalt contamination by continental crust: some experiments and models. *Contributions to Mineralogy and Petrology* **80**, 73–87.
- Watson, E. B. & Jurewicz, S. R. (1984). Behavior of alkalis during diffusive interaction of granitic xenoliths with basaltic magma. *Journal of Geology* **92**, 121–131.
- Watson, E. B., Sneeringer, M. A. & Ross, A. (1982). Dissolution of dissolved carbonate in magmas: experimental results and applications. *Earth and Planetary Science Letters* **61**, 346–358.